AGU PUBLICATIONS

JGR

Journal of Geophysical Research: Earth Surface

RESEARCH ARTICLE
10.1002/2015JF003499

Special Section:
Glacier Surging and Ice Streaming

Dynamics of thermally induced ice streams simulated with a higher-order flow model

D. J. Brinkerhoff[1] and J. V. Johnson[2]

[1]Geophysical Institute, University of Alaska Fairbanks, Fairbanks, Alaska, USA, [2]Department of Computer Science, University of Montana, Missoula, Montana, USA

Abstract We use a new discretization technique to solve the higher-order thermomechanically coupled equations of glacier evolution. We find that under radially symmetric continuum equations, small perturbations in symmetry due to the discretization are sufficient to produce the initiation of nonsymmetric thermomechanical instabilities which we interpret as ice streams, in good agreement with previous studies which have indicated a similar instability. We find that the inclusion of membrane stresses regularizes the size of predicted streams, eliminating the ill-posedness evident in previous investigations of ice stream generation through thermomechanical instability. Ice streams exhibit strongly irregular periodicity which is influenced by neighboring ice streams and the synoptic state of the ice stream. Ice streams are not always the same size but instead appear to follow a temperature-dependent distribution of widths that is robust to grid refinement. The morphology of the predicted ice streams corresponds reasonably well to extant ice streams in physically similar environments.

Key Points:
- A new ice sheet model produces ice streams through thermofrictional instability
- Membrane stresses lead to a unique distribution of ice stream widths
- Modeled ice streams exhibit a complex superposition of periodic time scales

Supporting Information:
- Movie S1
- Movie S2
- Movie S3
- Text S1 and Captions of Movies S1–S3

Correspondence to:
D. J. Brinkerhoff,
douglas.brinkerhoff@gmail.com

Citation:
Brinkerhoff, D. J., and J. V. Johnson (2015), Dynamics of thermally induced ice streams simulated with a higher-order flow model, *J. Geophys. Res. Earth Surf.*, *120*, 1743–1770, doi:10.1002/2015JF003499.

Received 24 FEB 2015
Accepted 5 AUG 2015
Accepted article online 9 AUG 2015
Published online 9 SEP 2015

1. Introduction

Ice streams are a conspicuous feature: they are often apparent in maps of surface velocity or surface elevation [*Joughin and Tulaczyk*, 2002], as well as through examination of morphological features at the ice surface such as shear margins and textural differences [*Echelmeyer et al.*, 1991]. Ice streams, in conjunction with other fast flowing outlet glaciers, are responsible for 90% of the drainage of the West Antarctic Ice Sheet [*Oppenheimer*, 1998; *Bamber et al.*, 2000] and account for a large proportion of the ice flux in East Antarctica and Greenland [e.g., *Rignot and Thomas*, 2002]. Ice streams also vary in time, potentially undergoing stagnation if the necessary conditions for streaming to occur are not satisfied [*Retzlaff and Bentley*, 1993; *Joughin et al.*, 2005; *Hulbe and Fahnestock*, 2007].

The putative mechanism for ice stream formation is a combination of thermomechanical and hydrologic feedbacks. *Fowler and Schiavi* [1998] showed that speedups could be initiated through the interaction of meltwater generation and sliding speed. Their model produced a "hydrologic runaway" effect, in which mutual feedbacks between sliding speed and meltwater generation sustained what they referred to as ''ice sheet surges". *Bougamont et al.* [2003] modeled the shutdown of Kamb Ice Stream using an advanced model of undrained till mechanics forced by basal freeze-on and melt. Other conceptual models invoke the necessity of basal water as a means for producing sliding but invoke transport into or away from the basin as a means for stream shutdown [*Alley and Anandakrishnan*, 1994]. *Price et al.* [2001] argue against this interpretation, however, suggesting that the evacuation of water from the basin of the stagnant Kamb Ice Stream is rather an effect of a more fundamental thermomechanical mechanism for ice stream shutdown, rather than a cause. *Sayag and Tziperman* [2008] show evidence that under a reasonable range of parameters, the case of water-enhanced sliding and its interaction with melt rates is fundamentally unstable, leading to ice stream development under small perturbations. Furthermore, under a multivalued sliding law, *Sayag and Tziperman* [2011] showed that two spontaneously generated streams can interact in complex ways, even demonstrating an apparently chaotic pattern of initiation and shutdown. In each case, streams persist so long as there is sufficient driving stress to overcome till friction and sufficient water to keep the till soft.

If it is assumed that ice can only slide over its bed if that ice is not frozen to its bed, then a necessary condition for streaming is a temperate bed. Through thermoviscous (heat generation due to internal deformation) and thermofrictional (heat generation due to basal sliding) feedback mechanisms the bed remains thawed, and the ice sheet continues to stream so long as heat sources can overcome the downward advection of cold ice.

Strain heating or basal sliding warm localized regions of an ice sheet, which in turn reduce viscosity or basal resistance, leading to still more deformation or sliding and so on. This classic example of a thermal runaway has been documented in several modeling studies [*Payne*, 1995; *Payne and Dongelmans*, 1997; *Payne et al.*, 2000; *Hindmarsh*, 2004a, 2009; *Saito et al.*, 2006; *Bueler et al.*, 2007].

We note that the two mechanistic categories of hydraulic runaway and thermal runaway are not exclusive. For water-related mechanisms of streaming to operate, the bed must be thawed. Conversely, a thawed bed suggests the presence of liquid water. The primary distinction is whether or not to elaborate on the mechanism of enhanced basal sliding beyond simply whether or not the bed is frozen. In this work, we adopt the latter mechanism and examine the formation of ice streams purely as a result of a step change in basal conditions (i.e., sliding versus not sliding) due to a change in the thermal state, without considering the specifics of ice water interaction. Due to the complexity and uncertainty evident in the subglacial hydrologic system [*Werder et al.*, 2013] and in particular its role in determining till strength and sliding speed [*Bougamont et al.*, 2003; *Tulaczyk et al.*, 2000], consideration of the specifics of the subglacial hydrologic system would prove challenging. Nonetheless, the interaction between hydrology and ice stream formation remains a fascinating potential line of inquiry.

Previous modelling studies have shown that in the presence of an abrupt change in basal traction, thermally driven oscillations can be produced. These oscillations exist in one-dimensional models and exhibit highly structured and periodic cycles of growth and decay [*Payne*, 1995]. In *Payne and Dongelmans* [1997], incorporation of a second map-plane dimension produced ice streams, but oscillations were suppressed. Oscillations returned and became irregular when an asymmetrical surface mass balance was included. The European Ice Sheet Modelling Initiative (EISMINT)-II benchmark experiments, in particular, Experiment H [*Payne et al.*, 2000], showed that most ice sheet models produce time-dependent, symmetry breaking streaming features which have been interpreted as spontaneously generated ice streams. EISMINT-II experiment F showed that ice sheet models can spontaneously generate instabilities purely through thermoviscous effects, without any basal sliding, but that these instabilities are steady in time.

Despite the fact that nearly all of the models in the EISMINT-II benchmark produced patterns characteristic of thermomechanical instability, persistent questions about the nature of these instabilities stymied their unqualified acceptance as physically meaningful. *Fowler* [2001] took issue with the use of a discontinuous sliding law in the context of the shallow-ice approximation (SIA), because it implies infinite local velocity gradients. Furthermore, *Hindmarsh* [2004a] proved that the thermomechanically coupled SIA was ill posed in the sense that the solution to such a problem does not converge to a unique solution under refinement of the numerical grid, for either the thermoviscous or the thermofrictional case. *Bueler et al.* [2007] showed that the instabilities generated under EISMINT-II F are "literally a numerical error" (while not necessarily discounting the physical validity of the thermoviscous instabilities). The patterns of enhanced flow evident in all of the above works exhibit grid dependence, wherein the particular structure of the numerical grid exerts a nonphysical influence on the model solutions due to imposed symmetries and preferential flow directions. *Saito et al.* [2006] showed that upon rotation of a steady state solution to the EISMINT-II F experiments away from this preferential grid orientation, the system immediately evolves back to its steady state.

Nonetheless, thermomechanical instabilities have elicited continued interest. *Saito et al.* [2006] showed that the thermoviscous instability is retained in the presence of membrane stresses (i.e., stresses that resist map-plane deformation) for the nonsliding case. *Hindmarsh* [2009] further showed that the inclusion of membrane stresses in the stress balance model yields an ice stream configuration that is robust under grid refinement. This trait effectively eliminates the issue of ill posedness. Additionally, for models in which basal occurs, the inclusion of membrane stress eliminates the problem of singular flux divergence at the boundary between sliding and nonsliding regions. Nonetheless, the results of both *Saito et al.* [2006] and *Hindmarsh* [2009] also show that the inclusion of membrane stresses does not alleviate grid dependence.

In this work, we build upon these previous advances to elucidate the dynamical and statistical properties of ice stream generation in an idealized case, utilizing model improvements that we argue allows physical conclusions to be drawn from the model results more confidently. In section 2, we present the equations of thermomechanically coupled ice sheet flow that form the core of a new numerical model. Section 3 introduces the experimental setup that we use to investigate the spontaneous formation of ice streams, which is modeled after EISMINT-II H. However, in contrast to previous studies, we include membrane stresses and use an unstructured computational mesh. We run the experiments under a variety of different assumptions

regarding environmental conditions, stress balance choice, grid resolution, and grid structure. In each of these experiments, thermomechanical instabilities lead to the spontaneous generation of ice streams. In section 4, we analyze the statistical properties of the model solutions. We first quantify the differences in time and space scales due to differences in surface boundary conditions. We then evaluate whether the morphological characteristics in the modeled ice streams converge to a stable distribution under the assumption of higher-order and shallow-ice dynamics. Finally, we examine the local-scale evolution of an individual ice stream. In section 5, we discuss the relevance of our results to extant ice streams and additional avenues for further experimentation.

This work is made possible by novel numerical methods for solving the ice sheet equations. These are described in Appendix A. In particular, we utilize the combination of a ς coordinate and a heuristic spectral element method to reduce the solution of the higher-order stress balance to a problem with fewer degrees of freedom in the map plane. This is coupled with a hybrid finite element/finite difference temperature model. We use an implicit/explicit decomposition of the flux vector to create a stable mass transport scheme. Much of the work evaluating the results of EISMINT-II type experiments came to a halt prior to the development of models that include membrane stresses alongside detailed energy balances and operating on unstructured grids. Here we return to an open problem in glaciology with a new model that is uniquely suited to further investigation into thermoviscous instabilities emerging from ice stream dynamics.

2. Ice Sheet Model

2.1. Model Equations

We model glacial ice as a shear-thinning and temperature-dependent fluid with a free boundary. There are three primary quantities of interest: the velocity field $\vec{u}(x, y, z, t)$, the ice thickness $H(x, y, t)$, and the temperature $T(x, y, z, t)$, where t is time, x and y are horizontally aligned Cartesian coordinates, and z is the vertical Cartesian coordinate. Note that we will also make use of cyclindrical coordinates $r = \sqrt{x^2 + y^2}$ and $\theta = \text{atan2}(y, x)$. In this section we describe the continuous equations employed in this work. The numerical methods used for the discretization and solution of these equations are given in Appendix A.

2.1.1. Velocity

The velocity field in an ice sheet is governed by momentum conservation. We assume that convective acceleration terms are negligible, leading to the Stokes equations. Furthermore, we assume that pressures are approximately hydrostatic and that vertical resistive stresses (stresses related to horizontal gradients of vertical velocities) are negligible. This leads to a well-known approximation to the Stokes equations alternatively known as the Blatter-Pattyn equations [*Pattyn*, 2003], the first-order equations [*Pattyn*, 2003] or the Multilayer longitudinal stresses (LMLa) [*Hindmarsh*, 2004b]. For consistency, and because in our discussion we will make reference to alternative schemes, we adopt the naming convention of *Hindmarsh* [2004b].

For a domain Ω with external boundary Γ, the LMLa equations are

$$\nabla \cdot 2\eta\dot{\epsilon} = \rho\vec{g}\nabla S \quad \text{on } \Omega, \tag{1}$$

where ρ is the ice density, g the acceleration due to gravity, η the ice viscosity, $\dot{\epsilon}$ the strain rate tensor associated with the LMLa equations, and S the ice surface elevation. The strain rate tensor is

$$2\dot{\epsilon} = \begin{bmatrix} 4\partial_x u + 2\partial_y v & \partial_y u + \partial_x v & \partial_z u \\ \partial_y u + \partial_x v & 2\partial_x u + 4\partial_y v & \partial_z v \end{bmatrix}. \tag{2}$$

The viscosity η depends on both the strain rate and the temperature

$$\eta(\dot{\epsilon}, T^*) = \frac{A(T^*)^{\frac{-1}{n}}}{2} \dot{\epsilon}_{II}^{\frac{1-n}{n}}. \tag{3}$$

T^* is the temperature corrected for the pressure dependence of the melting point and $\dot{\epsilon}_{II}$ is the (regularized) second invariant of the strain rate tensor. $A(T^*)$ is given by the piecewise Arrhenius relations

$$A(T^*) = \begin{cases} A_c \exp -Q_c/(RT^*); \text{if } T^* < 263 \\ A_w \exp -Q_w/(RT^*); \text{if } T^* \geq 263. \end{cases} \tag{4}$$

The surface boundary Γ_S is subject to a stress free condition:

$$2\eta\dot{\epsilon}\cdot\vec{n}=0 \quad \text{on } \Gamma_S, \tag{5}$$

where $\vec{n}$ is the outward unit normal vector. The basal boundary Γ_B is specified here as a general Robin boundary condition

$$2\eta\dot{\epsilon}\cdot\vec{n}=\vec{\tau}_b=f(\vec{u},T,H) \quad \text{on } \Gamma_B, \tag{6}$$

where $\vec{\tau}_b$ is the basal shear stress. f can be a function of thickness (or equivalently pressure, given the hydrostatic assumption), temperature, and basal velocity. We do not address the influence of marine boundaries in this work, so any lateral boundary (e.g., an ice cliff at the horizontal edge of the domain) is assumed stress free.

The vertical velocity w is found through mass conservation

$$\nabla\cdot\vec{u}=0, \tag{7}$$

after solving for the horizontal velocity components.

2.1.2. Thickness

Mass conservation is given by

$$\partial_t H+\bar{\nabla}\cdot\vec{q}=\hat{a}, \quad \text{on } \bar{\Omega} \tag{8}$$

where $\vec{q}$ is the depth-averaged flux vector and $\hat{a}$ is the effective mass balance (which for the sake of compactness includes both surface mass balance and basal melt). $\bar{\nabla}$ is the gradient operator restricted to the horizontal domain, and $\bar{\Omega}$ is the projection of Ω onto the horizontal plane. In this work, we only consider complete ice sheets, that is, geometric configurations in which there are no influx or outflux boundaries and in which the ice divide itself acts implicitly as a zero flux boundary condition.

2.1.3. Temperature

Temperature is found by solving the energy conservation equation

$$\partial_t T+\vec{u}\cdot\nabla T=\nabla\cdot\kappa\nabla T+\frac{\Phi}{\rho C_p}, \tag{9}$$

where κ is the thermal diffusivity, ρ is the ice density, C_p is the specific heat capacity of ice, and $\Phi=2\eta\dot{\epsilon}_{II}$ is the internal generation of heat due to strain. The temperature equation is also subject to the additional constraint that

$$T\le T_m, \tag{10}$$

where T_m is the pressure-dependent melting point. Additional energy generated in ice at the melting point is used to melt ice.

The model is completed by surface boundary condition

$$\kappa\nabla T\cdot\vec{n}=\frac{\alpha}{\rho C_p}(T-T_s) \quad \text{on } \Gamma_S, \tag{11}$$

where α is the heat transfer coefficient between the atmosphere and the ice sheet and T_s is the surface temperature, and the basal boundary condition

$$\kappa\nabla T\cdot\vec{n}=\frac{q+F}{\rho C_p} \quad \text{on } \Gamma_B, \tag{12}$$

where q is the geothermal flux and $F=f(\vec{u})\cdot\vec{u}$ is heat generation due to friction at the subglacial interface. When the bed is at the pressure melting point, excess heat contributes to the melting rate $\dot{M}$ as

$$\dot{M}=\frac{1}{\rho L}(q+F), \tag{13}$$

where L is the latent heat of fusion.

Table 1. Table of Experimental and Numerical Constants

Symbol	Constant	Value	Unit
A_c	Cold ice hardness	3.61×10^{-13}	$Pa^{-n}\ a^{-1}$
A_w	Warm ice hardness	1.73×10^{3}	$Pa^{-n}\ a^{-1}$
Q_c	Cold activation energy	6×10^{4}	$J\ mol^{-1}$
Q_w	Warm activation energy	13.9×10^{4}	$J\ mol^{-1}$
R	Gas constant	8.314	$J\ mol^{-1}\ K^{-1}$
γ	Melting point depth dependence	8.7×10^{-4}	$K\ m^{-1}$
ρ	Ice density	910	$kg\ m^{-3}$
g	Gravitational acceleration	9.81	$m\ s^{-2}$
n	Glen's flow exponent	3	
q_g	Geothermal heat flux	42	$mW\ m^{-2}$
κ	Thermal diffusivity	1.15×10^{-6}	$m^2\ s^{-1}$
C_p	Specific heat capacity	2009	$J\ kg^{-1}\ K^{-1}$
α	Heat transfer coefficient	10^{6}	$W\ m^{-2}\ K^{-1}$
$\dot{a}_{max}$	Divide accumulation rate	0.5	$m\ a^{-1}$
S_b	Accumulation gradient	10^{-2}	$m\ a^{-1}\ km^{-1}$
S_T	Surface temperature gradient	1.67×10^{-2}	$K\ km^{-1}$
R_{el}	ELA location	450	km

We do not include a separate thermal model for the bedrock, and geothermal heat flux is specified. We recognize that this assumption is certainly an oversimplification, particularly in cases exhibiting significant temporal variability. Nonetheless, we still use it in the interest of maintaining as simple a model as possible, with the understanding that the buffering effect of bedrock heat storage could have an effect on the time scales of heat transfer and that these effects are neglected in this work.

3. Numerical Experiments

3.1. Experimental Setup

Our numerical analysis of ice stream initiation is essentially based around the setup proposed in EISMINT-II experiment H [*Payne et al.*, 2000]. Parameter values are given in Table 1. The bed is flat, and we begin with a zero ice initial condition. The accumulation rate is defined by

$$\dot{a} = \min\left[\dot{a}_{\max}, S_b(R_{el} - r)\right], \tag{14}$$

where $\dot{a}_{\max}$ is the maximum accumulation rate, S_b is the horizontal gradient of accumulation rate, R_{el} is the radial location of the Equilibrium line altitude (ELA), and $r = |\vec{x}|$ is the radial distance from the center of the domain. Surface air temperature is given by a similar function

$$T_s = T_{\min} + S_T r, \tag{15}$$

where T_s is the surface temperature, $T_{\min}$ is the surface temperature at the ice divide, and S_T the spatial gradient of surface temperature with respect to r. Basal sliding is parameterized in the following way

$$\vec{\tau}_b = f(\vec{u}_b) = \begin{cases} \beta_{\text{low}}\vec{u}_b \text{ if } T = T_m \\ \beta_{\text{high}}\vec{u}_b \text{ if } T < T_m, \end{cases} \tag{16}$$

where $\vec{u}_b$ the velocity vector evaluated at the ice sheet base, $\beta_{\text{high}} = 10^9$ Pa a m^{-1}, $\beta_{\text{low}} = 10^3$ Pa a m^{-1}. This is essentially the same sliding law as specified in the EISMINT-II H experiment but formulated in terms of basal shear stress.

3.2. Variants

We ran two primary variants of this experiment: a warm experiment where $T_{\min} = 238.15$ K and a cold experiment where $T_{\min} = 223.15$ K. We used a mean mesh resolution of 12 km (defined in terms of mesh

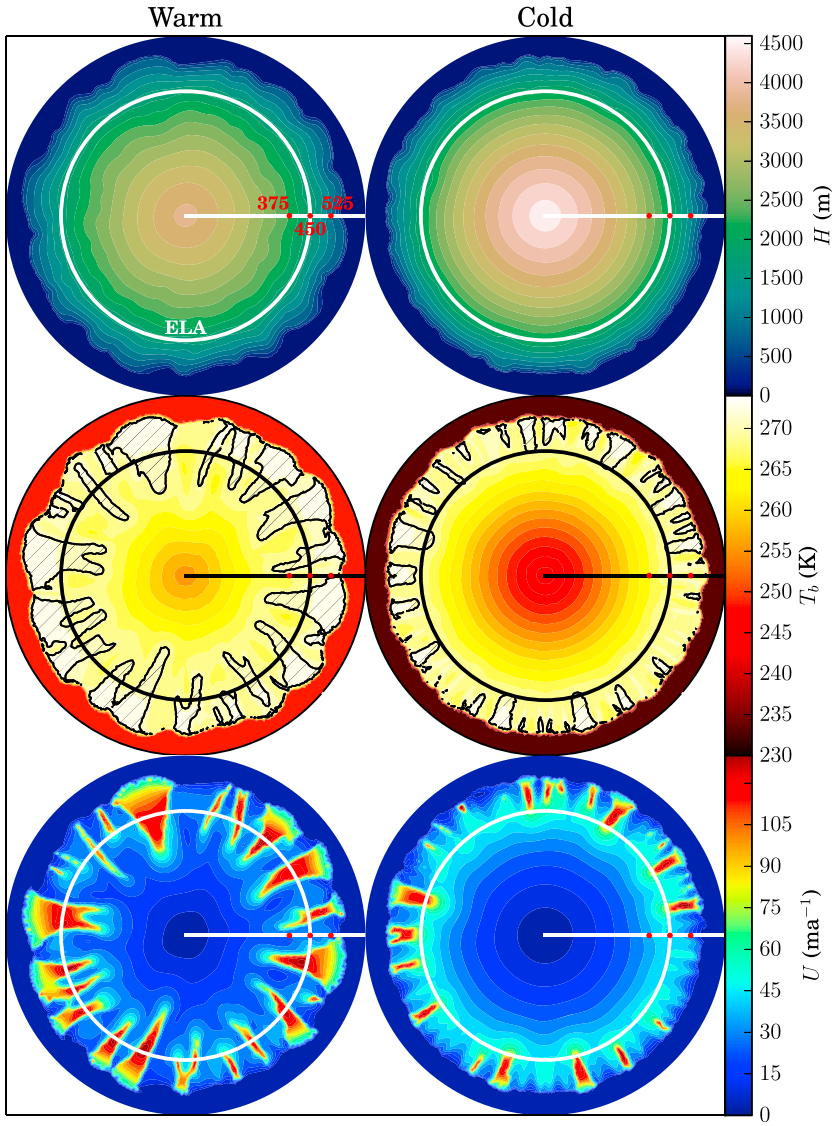

Figure 1. Thickness, basal temperature, and surface velocities at $t = 60$ ka. Red dots correspond to $r \in \{375, 450, 525\}$ km. Shaded regions of the temperature plot correspond to temperate basal conditions.

circumdiameter) for each of these cases. We also ran several subsidiary experiments, varying the mesh resolution between 50 km and 6 km and also whether the meshes were structured unstructured. We also ran each of these experiments with longitudinal stress gradients suppressed to evaluate the effect of membrane stresses on ice stream development and, in particular, to evaluate the relative degree of mesh dependence. Each experiments was run for 120 ka.

3.3. Meshes

Experiments using unstructured meshes were generated with GMSH [*Geuzaine and Remacle*, 2009]. The algorithm used by GMSH produces meshes with statistically uniform edge orientation. Structured meshes were also generated by GMSH.

4. Results

All experiments produce a spatially and temporally heterogenous pattern of flow, with strong symmetry breaking. Figure 1 provides images of the velocity, thickness, and basal temperature fields for both warm and cold experiments.

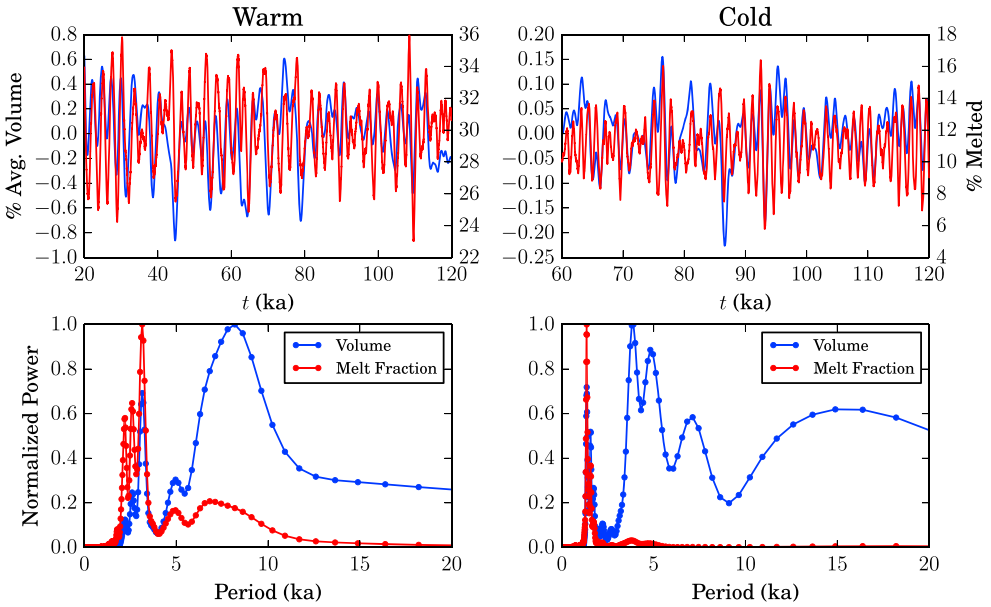

Figure 2. Time series and power spectra of total ice volume (blue) and melt fraction (red) for cold and warm experiments, following a spin-up period. Note the different time axis scales.

These images, while illustrating a representative sample of the spatial patterns of streaming generated by the model, do not demonstrate the complementary temporal variability. Complementary animations of model results are provided in Movies S1 and S2 in the supporting. A variety of qualitative phenomena are apparent. Streams initiate at locations of localized strain heating, and after reaching the pressure melting point, a positive feedback between sliding and frictional heat generation produces a localized increase in surface slope (or knickpoint) which migrates toward the ice divide, persisting until the reservoir supplying that ice stream possesses insufficient gravitational potential to continue to sustain itself, at which point it stagnates and its reservoir begins to refill.

It is also apparent that the streams interact with one another in a fairly complicated way. We see distinct instances of stream capture, in which two streams meld into one much larger stream (e.g., S1, NE corner, $t \in [31, 32.5]$ ka). It is also not uncommon to see streams with two distinct upper tributaries, neither of which appears dominant (e.g., S1, SE, $t \in [22, 25]$ ka). We also see another type of interaction between streams, in which streams with opposing deflection from the radial direction approach one another but do not entirely merge (e.g., S1, E-SE, $t \in [47, 49]$ ka).

4.1. Synoptic Variables Through Time: Evolution of Volume and Melt Fraction

We first take a synoptic view of the system's behaviour. Perhaps the two most relevant pieces of information in assessing the state of the experimental ice sheet as a whole are the normalized volume and melt fraction.

Figure 2 shows the proportional volume anomaly of the system following spin-up periods of 20 ka for the warm experiment and 60 ka for the cold experiment. The duration of the spin-ups were determined by finding the approximate location at which the linear trend in ice sheet volume became insignificant (i.e., the point at which the 1σ uncertainty for the slope parameter in a linear regression on volume includes zero). We see that the qualitative behavior for both is similar, predicting small scale irregular oscillations around a steady volume. These volumetric oscillations are on the order of 1% of the total volume of the ice sheet for both cases.

This is not to say that there is no cyclicity in the ice volume through time. In order to determine the time scales over which the cycles occur, we compute periodograms of the proportional volume anomaly and melt fraction. The periodograms were computed with Welch's method [*Welch*, 1967], using a Hann window with a window size of 40 ka and overlap of 90%. Figure 2 shows periodicity at time scales of around 3 ka and 9 ka for the warm experiment and 2 ka and 4 ka for the cold case, with additional small peaks elsewhere, as well as apparent diffuse low frequency variability, particularly for the cold experiment. Many of the spectral peaks are diffuse, indicating that periodicity is irregular.

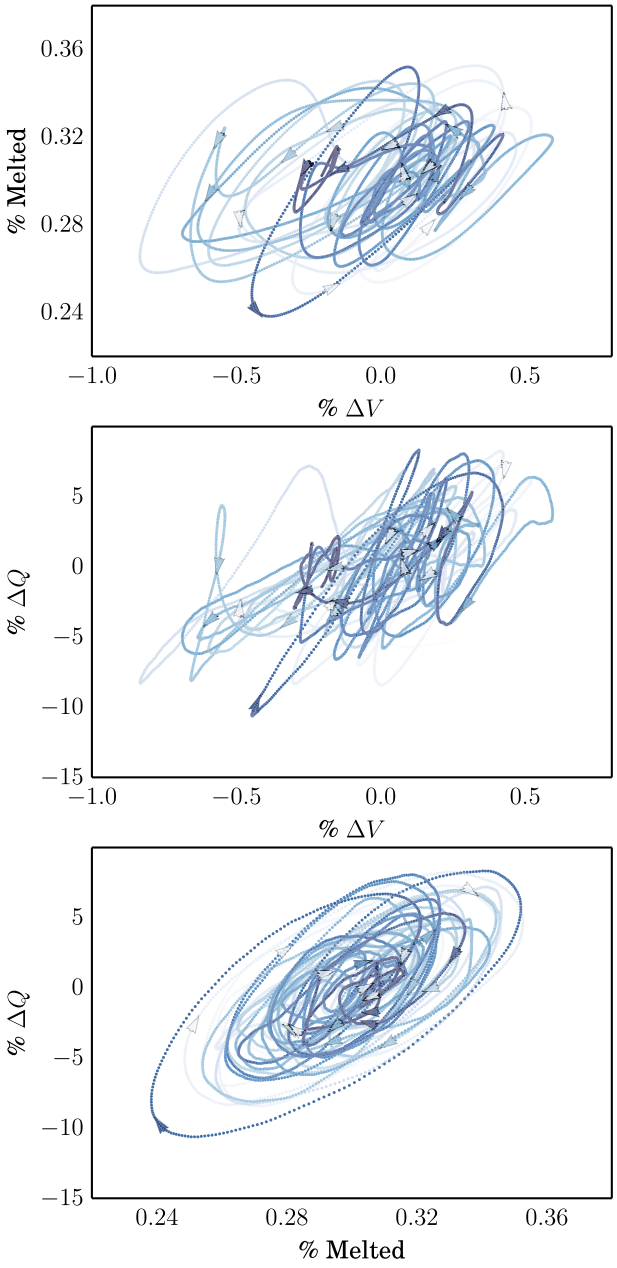

Figure 3. Phase plot for the three 10 ka intervals in $t \in [20, 50]$ ka. Arrows show the forward direction in time.

Short period volume spectra are coincident with the spectra of the melt fraction, which is also displayed in Figure 2, but long period variability in the melt fraction is much weaker. The melt fraction displays a larger amount of temporal variability than that reported in *Payne et al.* [2000], with a range of around 10% in the case of the warm experiment and 6% in the case of the cold experiment. This difference is explained by the inclusion of longitudinal stresses, which, as we will show subsequently, has the effect of producing more coherent and larger streams than the shallow-ice approximation. Note also that melt fraction and total volume are *positively* correlated, which is to say that at the maximum ice volume, the melt fraction is also at a maximum. This suggests that downwasting effects due to streaming are lagged relative to total ice volume.

This positive correlation can also be seen in Figure 3, which shows the phase plots of proportional volume anomaly, melt fraction, and average flux across the ELA. It is evident here too that a high melt fraction typically corresponds to a high volume and vice versa. However, the trajectory taken by the system when transitioning from low to high (in terms of both volume and melt fraction) is different from the trajectory taken from high to low. For increasing trajectories, melt fraction increases relatively slowly to start and then quickly increases once a sufficient volume has been reached. After this rapid increase in melt fraction, the system quickly deflates as ice is evacuated by high rates of basal sliding. Similarly, flux across the ELA is positively correlated with both but exhibits a much more predictable relationship with melt fraction than with volume, reflecting the stronger dependence of velocity on basal traction (and temperature) than on driving stress (and thickness).

A final point regarding the period of the volume and melt fraction is that the dominant time scales are temperature dependent. In particular, variability in ice volume and melt fraction due to the development of streaming features (the only source of temporal variability in the model) occurs on a shorter time scale in the cold experiments than in the warm ones. We will examine this more closely in subsequent sections.

4.2. Spatiotemporal Distribution of Ice Streams

All of the experiments that we conducted exhibit a complex spatiotemporal pattern, yet the ice sheet varies little in terms of synoptic variables, such as volume and melt fraction. This implies that the ice sheet is in dynamic equilibrium, undergoing oscillations around a stable attracting state [e.g., *Turcotte*, 1997]. However, examination of Figure 2 also indicates that the behavior of the system is not regularly periodic. That this

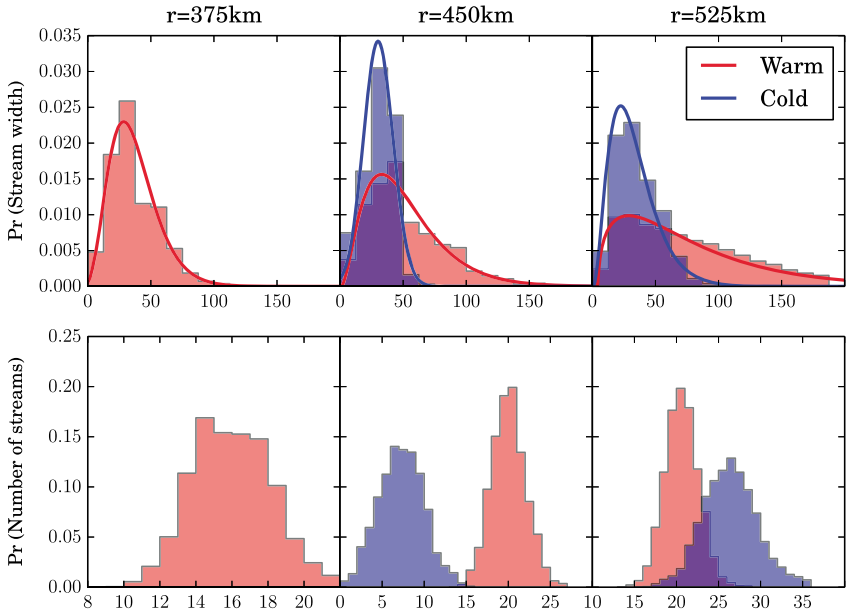

Figure 4. (top) Probability density of individual stream widths and (bottom) probability density of the number of discrete streams for (left) warm and (right) cold experiments. Additionally, overlain are the best fit lognormal distributions for stream widths.

irregularity exists is not surprising. There is no reason to expect that streams should orient themselves in such a way as to minimize their interactions with one another, and there are ample degrees of freedom with which to produce irregularities.

It is also clear that patterns exist and that the formation of streams is not random. For example, the number of active streams at a given time remains consistent within a certain range throughout the simulations (after the initial temperature-dependent transient). Similarly, streams exhibit consistent minima and maxima in terms of lateral and longitudinal extent. In light of the apparent unpredictability of the spatial patterns of streaming, it is useful to examine these features statistically. Figure 4 displays the empirical probability densities of ice stream width and number of ice streams for both the warm and cold experiments at $r \in \{375, 450, 525\}$ km distance from the ice divide. We define a sample point $\vec{r}_i$ as streaming if $\|\vec{u}(\vec{r}_i)\| - \|\langle\vec{u}(\vec{r})\rangle\| > 0$ and $T_b(\vec{r}_i, t) = T_m(\vec{r}_i, t)$. Stated more plainly, a sample location is streaming if it is moving faster than the average for its radial location and if the basal ice is molten. Data is only included for $t > 20$ ka for the warm experiment and $t > 60$ ka for the cold experiment, in order to eliminate the influence of the transient, ice sheet building stage of the simulation.

The warm simulation exhibits streaming at least to $r = 375$ km, but it is clear that there are fewer developed streams at this location compared to the locations further toward the margin. The number of streams at $r = 450$ km and $r = 525$ km is similar. For the cold experiment, there are no streams at $r = 375$ km and relatively few streams at $r = 450$ km. However, the number of streams rises sharply at $r = 525$ km.

Despite this, the mean number of streams near the margin in the cold experiment is 30% greater than the warm case. The mean stream width for the cold simulation is around 50% of the mean width of the warm simulation. They are also more consistent in size, with most streams falling in the range between 12 km (the lower detectable limit due to numerical resolution) and 100 km. Conversely, the warm experiment regularly produces streams of width greater than 150 km. For both experiments, the distribution of stream counts is nearly symmetric, while the stream width is right skewed. This skew is stronger for the warm experiment.

The reason for this dimorphism is a result of the smaller melt fraction in the cold experiment compared to the warm experiment. Vertical advection of colder surface ice cools a relatively larger portion of the bed, and the mechanism for enhanced basal sliding cannot operate as far upstream as in the warm case. Furthermore, this colder ice more strongly defines the interstream boundaries, leading to decreased width. Also, because increases in sliding speeds cannot propagate upstream as far, the reservoir of mass on which the stream can

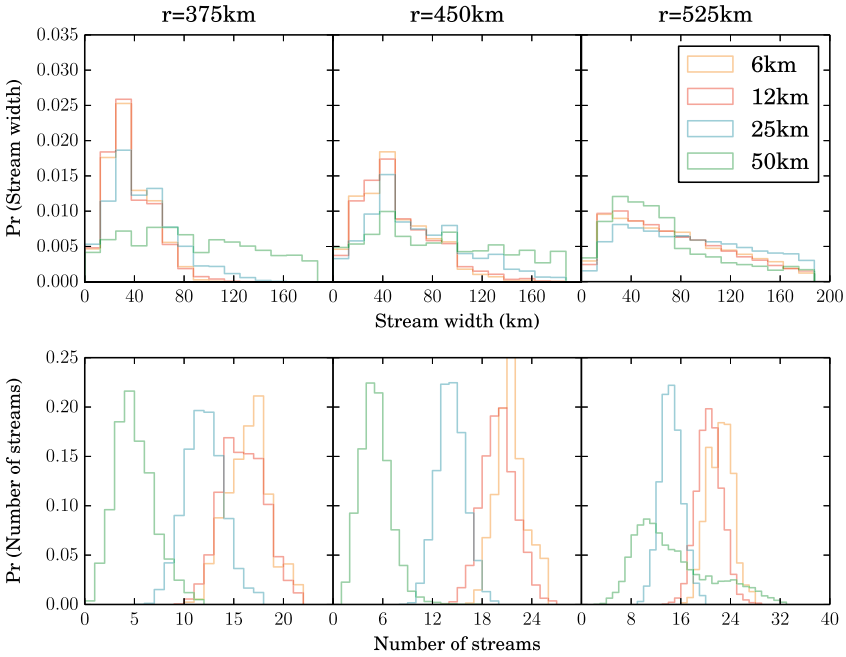

Figure 5. (top) Probability density of individual stream widths and (bottom) probability density of the number of discrete streams for the warm surface experiment at 50 km, 25 km, 12 km, and 6 km mesh resolutions.

effectively draw is smaller. This leads to a shorter lifespan for each stream. The reduced flux draw of each stream relative to total ice volume allows more streams to be supported simultaneously.

4.2.1. Spatial Resolution and Statistical Uniqueness

To assess the influence of grid size on the spatial distribution of streams, we ran the warm experiment using four different resolutions: 50 km, 25 km, 12 km, and 6 km. Figure 5 shows the histograms of stream widths and counts.

These distributions exhibit resolution dependence, particularly for the 50 km resolution experiment. This is not surprising, as the mesh resolution acts as a lower limit for observable stream size, yet we frequently see streams smaller than this developing in the higher resolution experiments. However, the distributions associated with the 25 km resolution experiment are similar to those of the higher resolution experiments. The 12 km and 6 km width distributions are almost indistinguishable, and the count distributions are similar. This is a key result, which indicates that once a critical resolution is reached, the spatial distribution of streaming features in this model is not dictated by grid size. Furthermore, the meshes are unrelated to one another. Nodes are not collocated, and there is no correlation between edge orientation. Because of this, we do note that under a two-sample Kolmogorov-Smirov test [*DeGrood and Schervish*, 2011], we reject the hypothesis that the distributions are identical. Nonetheless, the spatial distributions of ice streams are sufficiently similar to suggest that the distributions are converging toward a grid-independent result. Although the specifics of streaming flow in this context are mostly unpredictable, the statistical properties of streaming behavior exhibit statistically robust self-organization.

4.2.2. Effects of Grid Structure

In order to assess the effects of grid orientation on model results, we ran the 12 km warm experiment again but using a structured finite element mesh with the same mean element circumradius. The mesh was quadrilateral with crossed diagonals, which means that edges were oriented in four directions (e.g., N-S, E-W, NE-SW, NW-SE).

Discretizations produce a bias in the locations at which the model produces ice streams because the model tends to route flux along edges, and the positive feedback mechanism between flux and temperature acts preferentially when these edges align tangent to the primary flow direction. In the case of a grid with randomly oriented grid elements, this bias exists but is randomly distributed in space. Furthermore, a random grid does not impose any symmetry on the model solutions. In the case of the regular grid, we expect a bias along

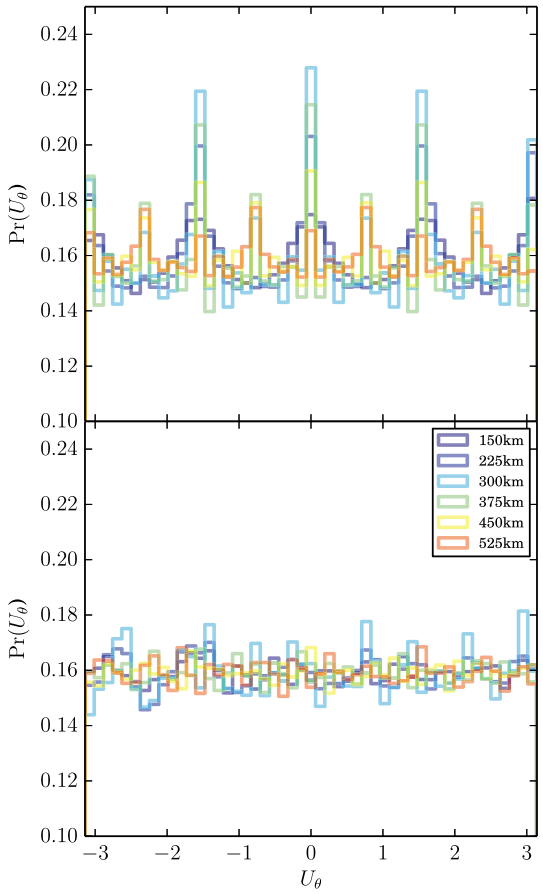

Figure 6. Probability density of flow directions for the 12 km resolution warm experiment using (top) structured and (bottom) unstructured grids at various radii. Warm colors are nearer the terminus.

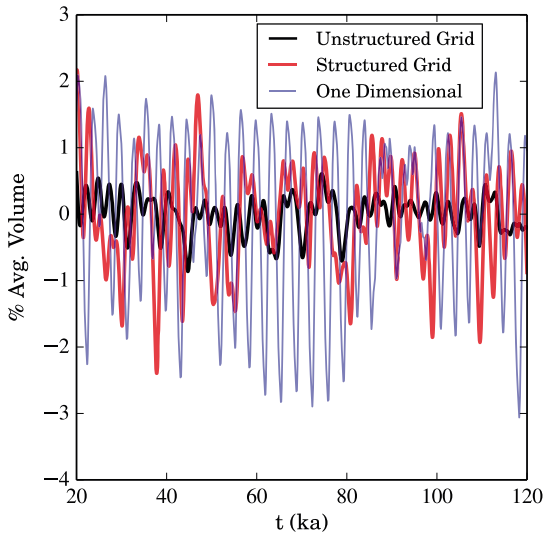

Figure 7. Volume time series for warm experiment at 12 km mesh resolution using an unstructured and structured meshes, as well as restricted to one horizontal dimension.

the principle directions of edge orientation. A crossed diagonal mesh produces eightfold symmetry, namely, mirror symmetry across each principle edge orientation.

Figure 6 shows probability densities for flow direction using both the structured and unstructured mesh. The bias toward the cardinal directions is evident in the case of the structured grid. This bias is stronger near the divide and becomes progressively weaker nearer the margin of the ice sheet. The unstructured mesh also shows a bias. However, this is distributed without a clear pattern and is of a lower magnitude than the structured case.

The effect of imposed symmetry is of more practical importance than the evident flow direction bias. The eightfold symmetry effectively reduces the number of degrees of freedom of the problem and causes at least eight streams to be synchronized. For the unstructured case, this lack of symmetry makes this synchronization less likely. As such, the standard deviation of the unstructured volume oscillations through time is 20% of that produced by the structured oscillations (Figure 7). Further, if we restrict the experiment to one spatial dimension, the oscillations become larger, with a standard deviation an order of magnitude larger than the unstructured case. Thus, a structured grid effectively reduces the dimensionality of the problem, and the results of such represent an intermediate case between the unstructured grid and the one-dimensional problem.

The orders of magnitude of the one-dimensional oscillations are similar to the analogous case in *Payne* [1995]. The small magnitude of oscillations for the unstructured grid relative to the structured or one-dimensional case is a result of the interaction between ice streams and the loss of symmetry. Since all of the ice streams draw upon a common reservoir, the evacuation of large amounts of ice by some streams has a tendency to shut down others, and this is done asynchronously. Put another way, for large variations in volume to occur,

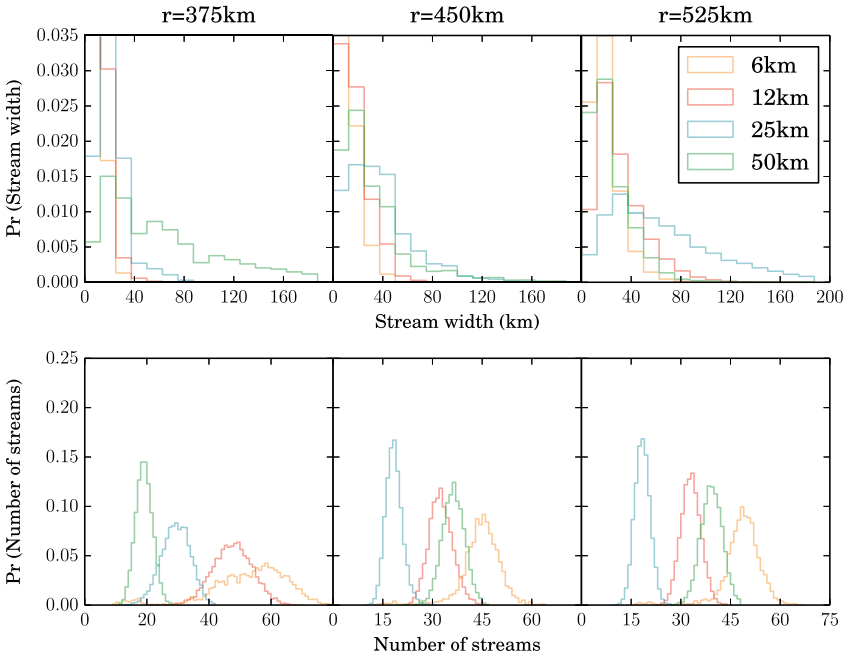

Figure 8. (top) Probability density of individual stream widths and (bottom) probability density of the number of discrete streams for the warm surface SIA experiments at 50 km, 25 km, 12 km, and 6 km mesh resolutions.

streams would have to exhibit resonance, their cycles of growth and purging being coincident. Due to the asymmetry in surface elevations, this does not occur and ice volume remains relatively constant.

4.2.3. Inclusion of Membrane Stresses

We can further assess the regularizing effect of membrane stresses by explicitly suppressing them and rerunning the experiments. Note that for these experiments, the only difference with the corresponding higher-order experiments is the suppression of the membrane stress terms in equation (1), leading to the shallow-ice approximation. Otherwise, the solution procedure is identical.

Figure 8 shows the stream width and stream count histograms for the shallow-ice approximation experiments. The evident convergence of the higher-order experiments is absent, and the statistical properties of the streams remain resolution dependent at the high resolutions where the LMLa model had converged to statistically unique values. Furthermore, the low-resolution experiment exhibits the curious phenomenon of producing more streams than the higher resolution experiments. This is because the lack of a structured grid does not possess favorable numerical pathways to develop coherent streams in the radial direction. Instead, the simulation produces a noisy velocity field where mass is routed down ephemeral local gradient maxima.

4.3. Temporal Patterns of Ice Stream Formation

In addition to assessing the aggregate statistical properties of simulated ice streams, we also seek to identify localized patterns in velocity, ice thickness, and the basal temperature as a means to better understand the dynamical mechanisms responsible for their formation. Figure 9 shows the warm-experiment time series (with membrane stresses turned on) of velocity at $r \in \{375, 450, 525\}$ km along the x axis. Note that the signal has had the mean value subtracted, so the figure is displaying velocity anomalies.

The first item of note is the strong irregularity in the observed cycles. Though streaming is oscillatory around a stable mean state, this local signal exhibits a less regular structure than do volume or melt fraction. This irregularity is evident when examining the power spectra of the signal, where we see dominant periods of ˜5 ka and 6 ka, but with considerable spread in these peaks, as was the case for the synoptic variables volume and melt fraction. Additionally, there are both longer and shorter period cycles superimposed upon the dominant one. Note that one of the additional spectra is concentrated around 9 ka, which is the dominant spectra in the volume time series for this experiment. This spectrum is most notable at the most upstream location. We interpret the appearance of this spectrum in the velocity signal to be the response of the individual stream to the overall state of the ice sheet. This is not the dominant local spectrum. Rather, the dominant spectra

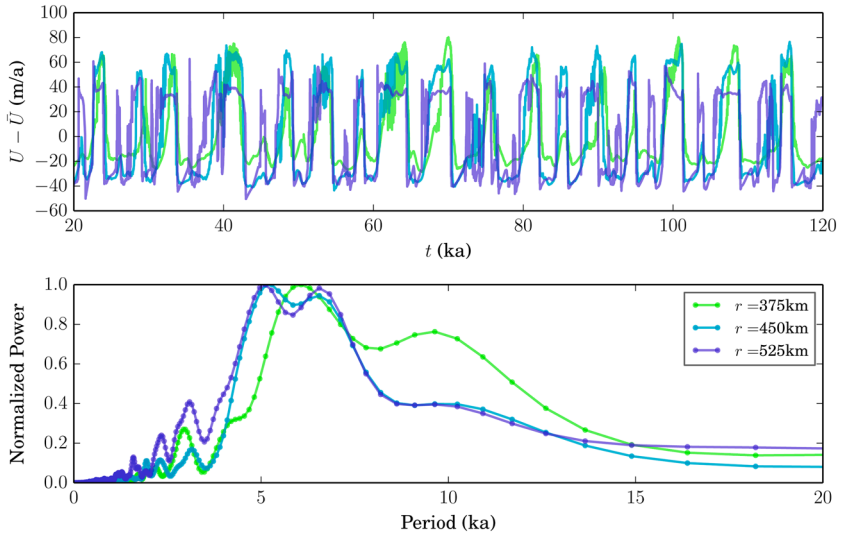

Figure 9. Time series and normalized power spectra for velocity at $\theta = 0$ and $r \in \{375, 450, 525\}$ km for the warm experiment at 12 km resolution.

are driven by the physics of the isolated stream, with higher-order effects being a combination of synoptic ice sheet conditions coupled with the behavior of neighboring streams exhibiting stream capture and basin depletion. The qualitative pattern of temperatures at the same location follows that of the velocity (Figure 10), and the temporal scales indicated by the spectra are similar.

Thickness, as shown in Figure 11, also exhibits similar spectra to velocity and temperature, further underscoring the coupling of the three. However, the thickness signal departs from the other two in that it lacks a discrete plateau; i.e., the thickness signal does not exhibit the obvious on/off type behavior that we see in temperature and velocity. This is because thickness is primarily diffusive and is not subject to the discontinuity induced in the velocity field by the change in sliding velocity and in temperature by the sudden presence of frictional heating. Also, it is interesting to note that although all three sample points were positively correlated in the other glaciological variables, for the thickness field, the lowest sample location exhibits a negative correlation: as material is evacuated from the accumulation area, it is deposited in the ablation area, increasing thickness. This effect has implications on driving stress evolution that we will discuss later.

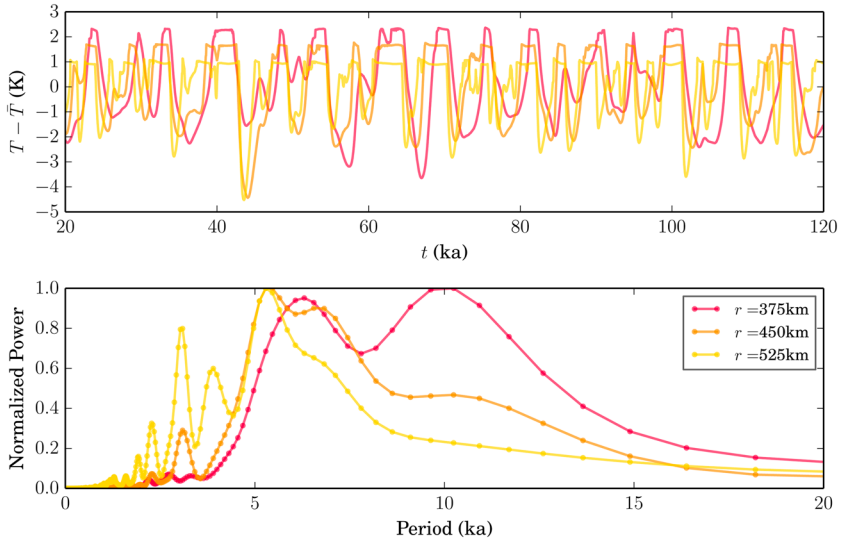

Figure 10. Time series and normalized power spectra for basal temperature at $\theta = 0$ and $r \in \{375, 450, 525\}$ km for the warm experiment at 12 km resolution.

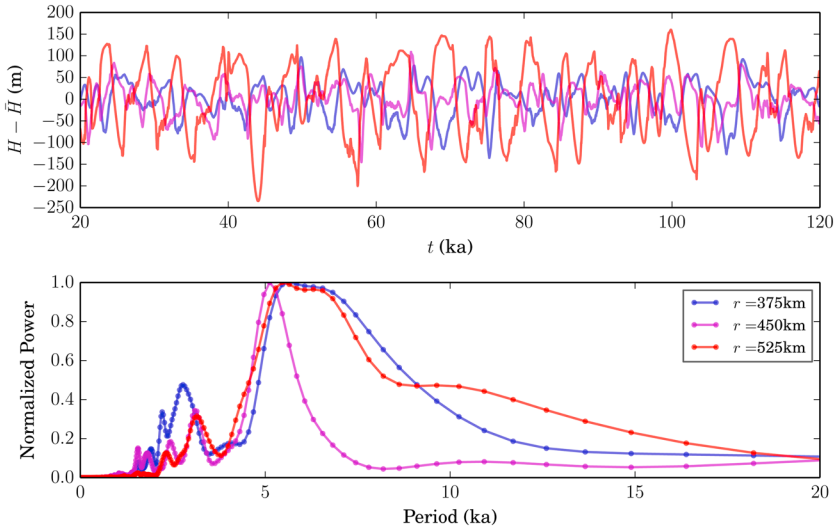

Figure 11. Time series and normalized power spectra for thickness, at $\theta = 0$ and $r \in \{375, 450, 525\}$ km for the warm experiment at 12 km resolution.

Equivalent plots for the cold simulation are presented in Figures 12–14. Many of the same phenomena are occurring, though on a shorter time scale. Additionally, as noted in previous sections, the spatial extent of the generated ice streams is smaller, and we see that the most inland sample location exhibits very little variability associated with streaming. Rather, the spectra tend to capture the synoptic scale variability of Figure 2. The coupling between this synoptic variability and the local variability is much tighter in the cold case, indicating either a stronger control of these synoptic processes on stream formation or a smaller influence of individual streams on synoptic scale processes or both. Curiously, between 90 ka and 105 ka, all variables exhibit a period doubling coupled with an increase in regularity, which does not occur elsewhere in the time series. This appears to coincide with a number of streams in close proximity to the sample locations all becoming in phase (see Movie S3). This further illustrates the potential for complex interactions between adjacent streams.

4.3.1. Relationship Between Glaciological Variables

The relationship between velocity, thickness, and temperature is illustrated by normalizing them and plotting them together over a shorter time period of 20 ka (Figure 15). At the downstream location, stream initiation occurs where the temperature reaches the pressure melting point and sliding is initiated. This speedup

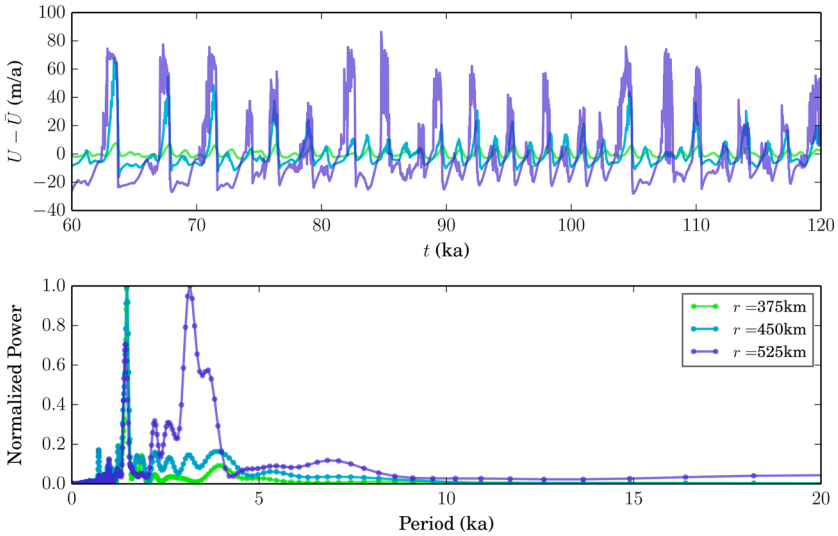

Figure 12. Time series and normalized power spectra for velocity at $\theta = 0$ and $r \in \{375, 450, 525\}$ km for the cold experiment at 12 km resolution.

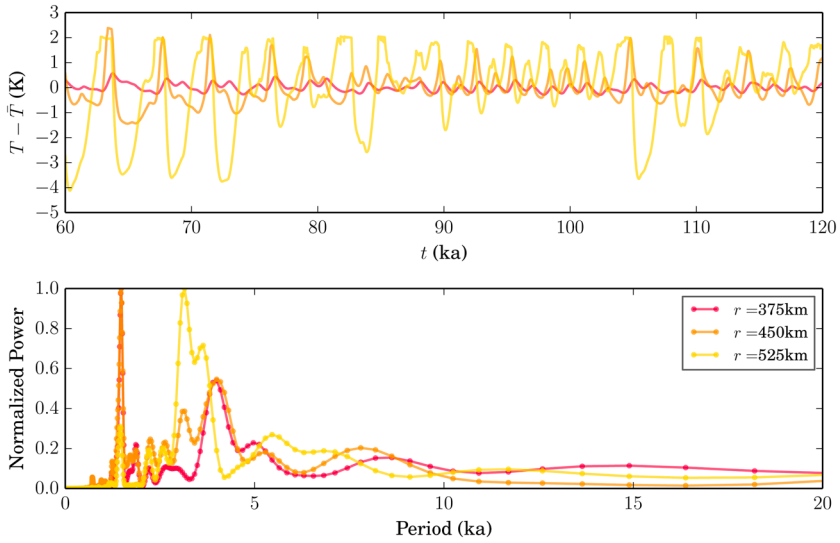

Figure 13. Time series and normalized power spectra for basal temperature at $\theta = 0$ and $r \in \{375, 450, 525\}$ km for the cold experiment at 12 km resolution.

propagates upstream. At the upstream location this mechanism is associated with a drawdown of ice and at downstream locations a buildup, as ice is rapidly transported from the accumulation zone to the ablation zone.

The characteristic times scales over which velocity, temperature, and thickness respond are distinct. Velocity responds to discontinuities in basal traction immediately, while temperature is more moderated, and thickness responds much more slowly. The high-frequency noise evident in the velocity field is a result of the rapid switching between temperatures at and just below the pressure melting point.

4.4. Dynamics of a Single Stream

The simulated ice streams are not static in the map plane, and as such observing the evolution of an ice stream at horizontally fixed points fails because the ice stream centerline rapidly migrates away from the observation point. Indeed, it is important to make the point that streams are not a consistent property of a parcel of ice. Individual pieces of ice may switch between being a constituent in an ice stream or not. In this sense, an ice stream behaves like a kinematic wave, which can have a propagation velocity quite distinct from that of the underlying material. In particular, the kinematic wave tends to move much more quickly than the underlying ice, both longitudinally [*Price et al.*, 2001] and laterally [*Echelmeyer and Harrison*, 1999].

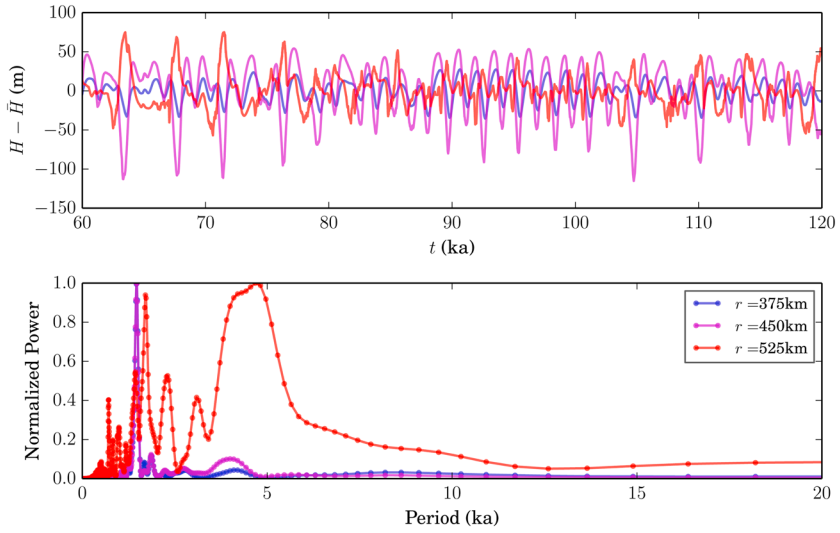

Figure 14. Time series and normalized power spectra for thickness at $\theta = 0$ and $r \in \{375, 450, 525\}$ km for the cold experiment 12 km resolution.

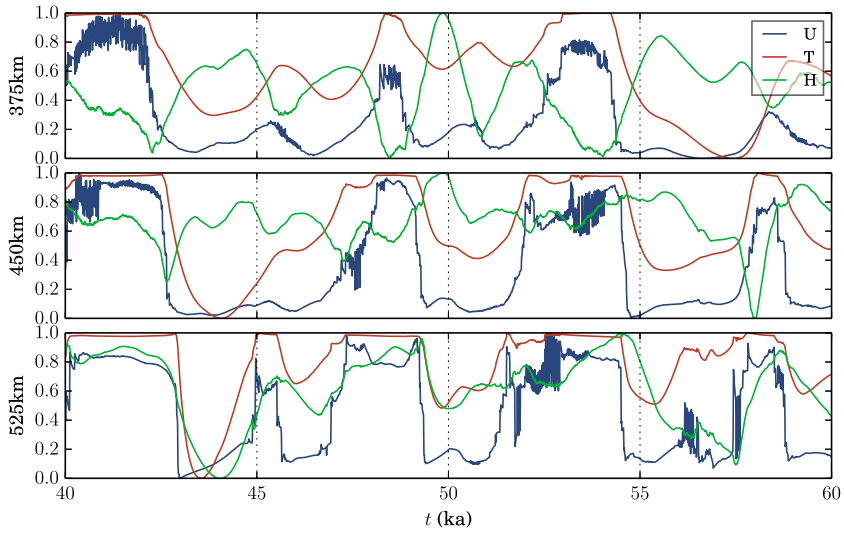

Figure 15. Time series over a 40 ka subset of glaciological variables velocity, thickness, and basal temperature at $\theta = 0$ and $r \in \{375, 450, 525\}$ km for the warm experiment at 12 km resolution.

To capture the evolution of a single stream, rather than the effect of that stream upon a fixed point, we plot the evolution of glaciological variables along the streamline that intersects the velocity maximum of a chosen ice stream from inception to stagnation. This plot is given by Figure 16 and corresponds to Movie S3. We chose a stream arbitrarily from the warm experiment at 6 km resolution, but experimentation has shown that most streams exhibit the same qualitative (and similar quantitative) evolution as that described here. Note that the plots show anomalies relative to the initial time, rather than absolute values.

The velocity plot illustrates the wave of increasing velocities propagating upglacier. This is also apparent in the temperature and thickness fields. This process of knickpoint migration occurs over approximately 3 ka, after which the ice stream remains in a stable, streaming configuration for an additional 1.5 ka. The stream then stagnates. The reduction in velocity to nonstreaming levels occurs over tens of years. The temperature field also decreases to prestreaming values, as the dominant frictional heat source is absent. The thickness upstream of the ELA begins to increase, while the accumulated ice below the ELA, no longer being supplied with mass from upstream, begins to downwaste.

5. Discussion

5.1. Physical Context

In the above sections, we have presented and analyzed the behavior of ice streams in a single and rather idealized context. In particular, we considered an ice sheet with uniform basal topography and a terrestrial terminus, which is of a similar size to West Antarctica. No locations on Holocene earth directly mirror these assumptions. The Greenland Ice Sheet's terrestrially and marine terminating glaciers tend to have strong topographic controls which fix the location of high flux features or are "isbræ" type [*Truffer and Echelmeyer*, 2003]. This is true of many outlet glaciers in East Antarctica as well. In West Antarctica, much of the underlying topography in streaming regions is flat [*Joughin et al.*, 2002], but ice streams are uniformly marine terminating.

There are several qualitative differences between our model setup and the ice stream configurations stated above. Topography can exert a strong control on the location of fast flow features, and topographic control constitutes a primary difference between ice streams and isbræ. In the case of the latter, we expect that topographic controls would mitigate much of the lateral migration of ice streams exhibited in our simulations. On the contrary, both *Payne* [1995] and the one-dimensional simulations presented in this work suggest that lateral confinement would not eliminate cyclicity. The underlying mechanism of streaming (i.e., the thermomechanical feedback between sliding and temperature) remains valid, even in the presence of constraints on lateral motion.

We also postulate that the choice of simulating a terrestrial margin introduces additional irregularity into the periodicity of ice stream growth and stagnation. In the terrestrially terminating case, the terminal lobe acts

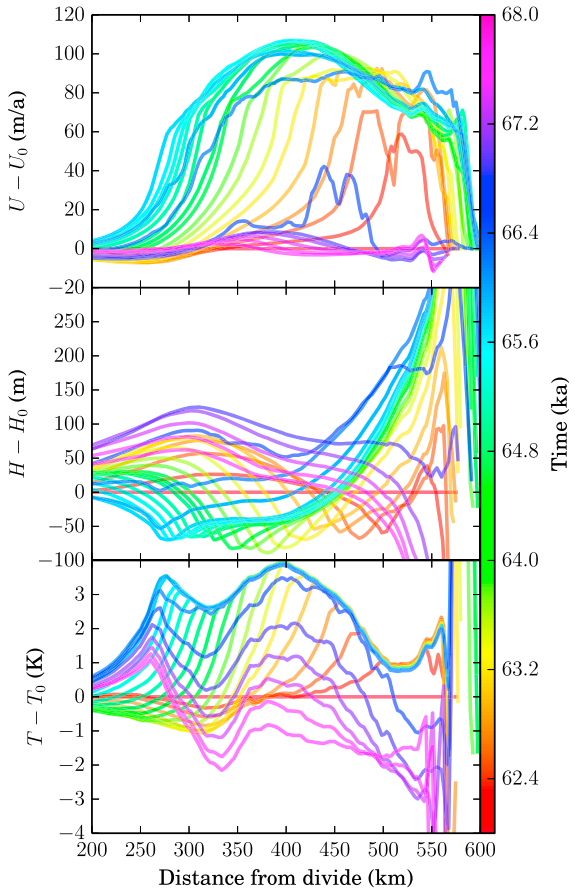

Figure 16. Velocity, thickness, and temperature along the centerline of an ice stream from inception to stagnation.

in a way rather analogous to a delta in fluvial systems or a piedmont glacier, with an excess of ice accruing in regions without lateral confinement. In the case of fluvial deltas, routing of flow exhibits chaotic properties, as the prograding of sediment continuously makes flow paths less energetically favorable [*Seybold et al.*, 2007]. Piedmont glaciers also exhibit complex spatiotemporal velocity and thickness patterns, which is apparent both from observations of morainal deposition and to altimetry [*Muskett et al.*, 2008]. The chaotic processes inherent in these "depositional" environments may propagate into upstream environments as well. A marine outlet, in which excess mass leaves the system efficiently through the calving process, may not exhibit the same degree of irregularity.

Nevertheless, the simulated ice streams possess many qualitative and quantitative similarities with extant observed ice streams, despite the differences in boundary configuration. The ice streams generated by the model are roughly consistent in size (50–150 km width and 300 km length) and velocity (150 km a^{-1}) relative to the Siple Dome ice streams [*Joughin et al.*, 2002], as well as the Northeast Greenland ice stream. Additionally, the spacing of the streams is similar. This is encouraging when we consider that the mean annual temperature at the WAIS divide is similar to the divide temperature used in the warm simulation (244.5 K [*Orsi et al.*, 2012] verbs 238 K, respectively). Lateral stream migration rates are of the correct order of magnitude (10–100 m/a) relative to Kamb Ice Stream [*Echelmeyer and Harrison*, 1999; *Bindschadler and Vornberger*, 1998]. We acknowledge, however, that the spatial resolution of the model is probably too coarse to capture the specific dynamics associated with shear margins. However, the localized high rates of shear strain heating are still the mechanism by which this migration occurs in the model.

Colder East Antarctic ice streams are smaller in both width and longitudinal extent, as are the streams produced by the cold experiment. Alternative mechanisms such as differences in till properties or basal geometry could also explain the difference between West and East Antarctic ice streams; however, thermal factors seem likely to play a role as well. On a side note, the assumptions of terrestrial termination and lack of topographic confinement would be reasonable for simulations of Pleistocene ice sheets. The Laurentide and Fennoscandian ice sheets possessed land terminating ice streams [e.g., *Stokes and Tarasov*, 2010], and these results are applicable to those cases. In the context of one of the large Pleistocene ice sheets, a flat bed is also a reasonable approximation.

The simulated ice streams exhibit the localized poststagnation buildup and flux rerouting that is currently though to be observed between ice streams Kamb and Whillans [*Price et al.*, 2001; *Conway et al.*, 2002], further evidence that if not the specific quantitative details, then at least many of the qualitative phenomena are being correctly reproduced by the model. Empirical and theoretical studies have shown that the shutdown process should take 50–150 years [*Retzlaff and Bentley*, 1993; *Alley and Anandakrishnan*, 1994], and the stagnation time of the ice streams modeled in this work is of the same order. We do note, however, that the results of the studies mentioned were predicated on the assumption of dewatering and subsequent restrengthening of the till bed as a means for ice stream shutdown, while we rely on basal refreezing. Despite this,

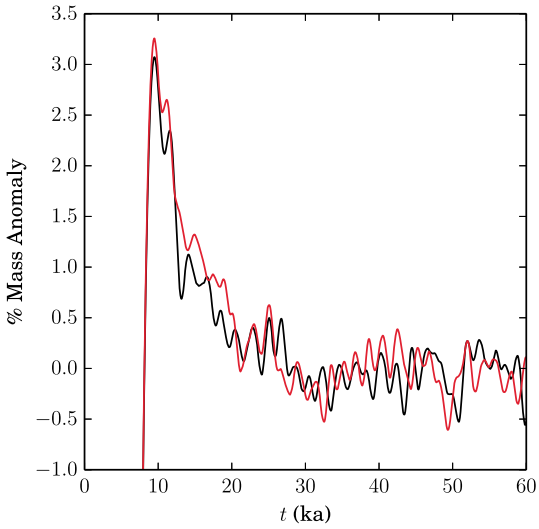

Figure 17. Volume evolution of the 12 km resolution experiments initialized with a small perturbation in initial thickness. The divergence of the two trajectories implies sensitive dependence on initial conditions.

both mechanisms couple basal sliding with thermodynamics in a similar way, so it is probable that the effects shown in this work would occur under both assumptions.

Nonetheless, a useful line of further inquiry would be to explicitly couple the ice dynamics model presented here with a more complex model of thermomechanically coupled till deformation. Such an experiment could be extended even further with the inclusion of an explicit model of subglacial hydrology [e.g., *Flowers*, 2015], which could be used to drive a dependency of sliding speed not only on basal thermal conditions but also on subglacial water pressure.

5.2. Chaotic Dynamics

The lack of regular periodicity exhibited by the model solutions coupled with its tendency toward dynamic equilibrium both provide a compelling implication that the dynamics of thermally driven ice stream formation are chaotic. While it is not possible to rigorously prove this, there are three necessary properties for a system to be thought of as chaotic [*Banks et al.*, 1992].

The first property of a chaotic system is that it should have dense periodic orbits. Stated simply, given enough time, any trajectory in the phase space should be approached arbitrarily closely by another at a later time. This provides the criterion that the region of feasible states is bounded and that oscillation occur around a stable region. This is evident in Figure 3, where despite exhibiting complex behavior, the trajectories remain within a certain distance of one another.

The second property is that the system should exhibit topological mixing or that given two arbitrarily close trajectories sampled a long time after chaotic dynamics have been initiated, one should not be able to determine anything about the initial conditions. While this is hard to show independently, we can make use of the fact that this property in conjunction with the first implies sensitive dependence on initial conditions [*Banks et al.*, 1992], which is the most well-known property of chaotic systems, and is much more straightforward to see from empirical results.

Sensitive dependence on initial conditions implies that for an arbitrarily small perturbation in initial conditions, the state of the trajectory of the perturbed system will depart exponentially quickly from the trajectory of the unperturbed system. For simpler systems, this can be quantified with Lyapunov exponents and other analytical devices. In our case, this is not possible. Nonetheless, we can evaluate whether this property holds experimentally by imposing two very similar initial conditions and seeing whether the trajectories of the system diverge. In our case, we compared the results of two 12 km resolution warm-experiment runs, for each of which we perturbed the initial thickness by a normally distributed random value with standard deviation of 0.1 m. These perturbations are 4 orders of magnitude smaller than the mean thickness of the simulation. The volume time series of these two experiments are shown in Figure 17. Note that these trajectories diverge immediately upon the commencement of streaming behavior at around 8 ka. A similar result would certainly occur if we used the same initial condition but used a different (though statistically equivalent) mesh.

We reiterate that we cannot show for a fact that the thermomechanically coupled system of equations presented in this work exhibit chaotic dynamics. Nonetheless, all signs point to such a conclusion. This working hypothesis provides potential interesting lines of further inquiry. In particular, it would be interesting to examine the bifurcation properties of the system. For example, it is obvious that the thermofrictional instability could not produce chaotic dynamics if the bed was uniformly temperate. The same is true in the opposite case; if the bed remains uniformly cold, then the differences in sliding speed that produce the patterns examined here could not form. Thus, there is an intermediate temperature regime under which interesting dynamics can

occur. There are several questions about this region that could be pursued. First, how large is it? The region is clearly bounded above by the melting point, but what temperature conditions need to be imposed to avoid chaotic dynamics altogether? Second, at the boundaries of the chaotic region, do we see the typical signs of breakdown into chaotic behavior, such as the generation of limit cycles with period doubling? Third, how are these properties affected by other parameters, such as accumulation rate? With the growing understanding that chaotic dynamics are likely feasible in glacial systems [*Kingslake*, 2015; *Sayag and Tziperman*, 2011], answering these questions might give us a better means of predicting in what contexts ice stream initiation and stagnation, along with other dynamical phenomena like surging, might be expected.

5.3. On the "Ill-Posedness" of Thermomechanical Instabilities

As stated convincingly in *Bueler et al.* [2007], any feature that breaks the radial symmetry of our perfectly radially symmetric continuum problem is undeniably an error. However, we echo *Bueler et al.* [2007] in positing that this instability possesses physical relevance, rather than just numerical relevance. Indeed, the validity of this paper is predicated upon this assumption. Doing so is valid because, as is obvious, we are not solving the continuum problem, with all of its radial symmetry. Rather, we are solving a complementary discrete problem thereto, and this discrete approximation is explicitly (and deliberately) nonsymmetric. This nonsymmetry in the mesh provides the initial symmetry breaking that causes the thermomechanical instability to operate, and due to the exponentially increasing nature of the instability, we would be deeply concerned about our numerical results if these features did not appear. The lack of a thermomechanical instability would be a strong indicator of an overly diffuse numerical scheme. Furthermore, analytical results from *Hindmarsh* [2004a] and *Sayag and Tziperman* [2008] effectively show that the symmetric solution is unstable.

As exhibited by both *Payne and Dongelmans* [1997] and *Payne et al.* [2000], as well as proved by *Hindmarsh* [2004a], the shallow-ice approximation exhibits strong grid dependence, though the results of *Bueler et al.* [2007] appear to contradict this to some degree. We note that our work tends to support this notion of sensitive grid dependence. This is interpreted as some form of ill posedness, in the sense that the spatial error modes are not dissipated with increasing grid refinement, and the model fails to select a unique stream size. This is precisely the type of nonconvergence exhibited in Figure 8. *Hindmarsh* [2009] showed that the inclusion of membrane stresses causes streaming features to become robust with respect to grid refinement. Our work supports this conclusion, with the distribution of simulated ice streams converging to a unique distribution under grid refinement.

An issue not addressed by previous workers is the influence of grid orientation on the spatial distribution of ice streams. The influence of a regular grid, with cells oriented normal to the Cartesian planes, is evident in the thermoviscous features presented in *Payne and Dongelmans* [1997], *Payne et al.* [2000], *Bueler et al.* [2007], and *Hindmarsh* [2009]. In all of the above, flow direction in at least some streams was along the grid maximum. This influence was further demonstrated by *Saito et al.* [2006], who showed that thermoviscous instabilities returned to their preferred grid-oriented configuration after being rotated. We ameliorate this problem by using an unstructured grid that possesses the verified property of uniformly distributed edge orientations. We assert that this feature is critical to the conclusions of this paper; if we are to ascribe physical meaning to behavior that is brought about by a discretization error, then we must at least attempt to make those errors random, rather than systematic. Indeed, we find that the imposition of symmetry through discretization method has the notable quantitative effect of increasing the variability in ice sheet volume by a factor of 5.

6. Conclusions

We applied a new thermomechanically coupled ice sheet model to the problem of ice stream generation on a flat plane, subject to radially symmetric temperature and surface mass balance. We incorporated a discontinuous, temperature-dependent sliding law, which is well known to produce oscillatory streaming behavior. We ran two primary experiments, varying between them only the surface temperature in order to isolate this as a mechanism for producing differences in model behavior.

As in previous studies, we found that small perturbations to an otherwise radially symmetric ice sheet induce symmetry breaking and subsequent streaming behavior. This streaming behavior varies strongly in space and time, producing a variety of phenomena over spatial and temporal scales comparable to observations. Major examples include ice stream stagnation and flux capture. We find that the interaction of the cycles of individual ice streams coupled with interference from neighboring streams and the state of the ice sheet as

a whole produces irregular cycles which are somewhat unpredictable and yet stable in the sense of a chaotic attractor. The time scale of these cycles is temperature dependent but for the experimental setup considered here is on the order of thousands of years. The end of a streaming cycle is marked by a sudden stagnation over hundreds of years. Additionally, we find that streams exhibit temperature dependence in terms of size and frequency; warmer ice sheets produce larger and more long lived streams and are characterized by more variance in the statistical distribution of widths. Finally, we find that our model produces a kinematic wave-like propagation of streaming that corresponds with previous theoretical and conceptual models of ice stream generation and shutdown.

Our numerical scheme differed from previous work in a few key aspects. First, we included membrane stresses. This has the important effect of causing ice streams to select a unique minimum width, rather than becoming increasingly narrow, as is the case for (shallow-ice) models that neglect these stresses. To test this, we ran model experiments under progressively increasing numerical resolution and found that the statistical distribution of stream width and frequency approximately converges. Second, we utilized an unbiased and unstructured grid. This eliminates nonphysical symmetries imposed upon the modeled ice streams by the use of a structured grid. These symmetries effectively reduce the dimensionality of the problem, which causes larger fluctuations in synoptic variables such as melt fraction and total ice volume than is exhibited by model solutions computed using the unstructured grids.

The streams produced by these experiments appear similar in configuration, size, and longevity to observations of extant ice streams in Antarctica and Greenland, despite important differences in basal and terminal boundary conditions. The modeled ice streams exhibit many similar qualitative phenomena, such as stream capture and the propagation of kinematic waves upstream during shutdown. Even our simple model setup produces rich dynamics, including what appears to be mathematical chaos, and could serve as a base for further discussions of the statistical and dynamical properties of ice streams.

Appendix A: Numerical Methods

The following section contains technical information regarding the numerical methods used in solving the governing equations. We use a variety of novel techniques in order to make long-time integration of the higher-order thermomechanically coupled stress balance tractable. All finite element computations are performed with FEniCS [*Logg et al.*, 2012], with linear algebra handled by PETSc [*Balay et al.*, 2014].

A1. Numerical Solution of LMLa

Despite the efficiency of both the shallow-ice approximation (SIA) and shallow-shelf approximations (SSA), neither is suitable for holistic ice sheet modelling nor modelling of such transitional areas as shear margins and grounding lines. Nonetheless, it is often prohibitively expensive to solve the LMLa equations. Modelers have thus sought a model that retains something of the explanatory power of the first-order equations while retaining the low computational cost of the SSA.

Several models have accomplished this to some degree through a variety of means. For example, *Bueler and Brown* [2009] utilize a heuristic combination of the SSA and the SIA, weighting a linear combination of their solutions based on local conditions. However, the most commonly employed practice for reducing the dimensionality of the LMLa equations while retaining better accuracy than either the SIA or SSA is the depth integration of the LMLa equations coupled with a parameterization of the vertical or basal shear stresses. *Hindmarsh* [2004a] coined the term "L1L2" to refer to these types of models. *Pollard and DeConto* [2012] derived such a model, solving for the depth-averaged velocity while using the stress balance to produce an approximation to the basal velocity. The depth-averaged velocities were iteratively corrected with a Picard-type scheme. *Schoof and Hindmarsh* [2010] produced a depth-averaged model that solved for surface velocity and iteratively corrected the vertical shear. They also rigorously showed the order of accuracy of these approximations under different flow assumptions and showed that in areas of high slip ratios, the L1L2 model is not appreciably different from the Stokes model. Its accuracy relative to this model is only degraded in the high aspect ratio, low slip context. *Goldberg and Sergienko* [2011] derived another model that was formulated in terms of depth-averaged velocities and iterative corrections to the shear stress and showed that it compared favorably to the LMLa and the Stokes formulations at all but the shortest wavelengths and low slip ratios, echoing the theoretical results of *Schoof and Hindmarsh* [2010]. Both *Bassis* [2010] and *Schoof and Hindmarsh* [2010] show that this class of models is energy conserving (a necessary condition for declaring it physically tenable) by deriving the associated variational principles.

In the model presented in this work, we take an alternative approach to the same problem. Rather than making approximations to the LMLa scheme in its continuous form, we instead select a discretization of the unreduced system of equations that provides the desired numerical properties. Specifically, we use a method of weighted residuals with linear Lagrange finite elements in the horizontal dimension and a heuristic ansatz in the vertical dimension, which takes advantage of the predictable structure of the vertical velocity in ice sheets. In so doing we overcome two notable limitations of the L1L2 model, namely, its poor performance under low slip ratio, high aspect ratio conditions and inability to handle thermomechanical effects while retaining or perhaps improving upon its computational efficiency due to the availability of Newton's method.

A2. Comparison to L1L2

First, the heuristic methods used to derive the L1L2 system typically lead to an elliptic system with a corrective term that is incorporated through a fixed-point iteration [e.g., *Goldberg and Sergienko*, 2011 [2011, equations (41)–(44)]]. Fixed-point iterations exhibit linear convergence compared to the quadratic convergence rates of Newton's method. With methods for computing the analytical Jacobian necessary for Newton's method available, we find that there is great utility to casting the physical system as a set of coupled equations amenable to analytical differentiation. The model presented in this paper formulates the depth-averaged stress balance as a system of four or more equations, representing depth-averaged velocities corrected by vertical strain rates. This system is solved simultaneously using Newton's method. On a related note, when written as a system of simultaneous equations, it is straightforward to derive adjoint equations, either by hand or by automatic differentiation, which can be used for data assimilation or sensitivity analysis.

Second, depth-integrated models typically make the assumption that the vertical averages of strain rates (and by extension viscosity) are a sufficient approximation to the true vertical integral of the horizontal stress divergence. As demonstrated by *Schoof and Hindmarsh* [2010], this approximation holds in the high slip ratio context at all aspect ratios and in the low slip ratio case at shallow aspect ratios. It does not hold when aspect ratios are high and the slip ratio is low. Rather, our model uses numerical quadrature combined with a polynomial ansatz and can accommodate a vertically varying viscosity term in the membrane stresses. This also allows us to include a vertically varying temperature field with a reasonable amount of degradation in accuracy relative to the LMLa equations, a critical feature if this stress balance is to be used for polythermal ice.

A3. Weak Form and ς Coordinate

In order to solve equation (1) using weighted residual methods, we write it in weak form and simultaneously adopt a ς coordinate [e.g., *Pattyn*, 2003], defined by

$$\begin{aligned} \hat{t} &\rightarrow t \\ \hat{x} &\rightarrow x \\ \hat{y} &\rightarrow y \\ \varsigma &\rightarrow \frac{S-z}{H}. \end{aligned} \tag{A1}$$

Introducing a test function Π, the weak form of the LMLa equations is to find $\vec{u} \in U$ such that

$$\begin{aligned} &\int_{\bar{\Omega}} \int_1^0 \left[\bar{\nabla}\Pi + \partial_\varsigma \Pi \nabla \varsigma\right] \cdot 2\eta \dot{\epsilon} H \mathrm{d}\varsigma \mathrm{d}\bar{\Omega} \\ &+ \int_{\bar{\Omega}} \left[\Pi \cdot f(\vec{u}, T, H)\right] |_1 \mathrm{d}\bar{\Omega} - \int_{\bar{\Omega}} \int_1^0 \Pi \cdot \vec{\tau}_d \mathrm{d}\varsigma \mathrm{d}\bar{\Omega}, \\ &\forall \Pi \in V, \end{aligned} \tag{A2}$$

where $U = V = H^1(\Omega)^2$ and $\vec{\tau}_d = \rho g H \nabla S$ is the gravitational driving stress. We have substituted relevant boundary conditions.

A4. Discretization

We use two distinct orthogonal basis sets for the horizontal and vertical dimensions. Our choice of vertical basis is motivated by four criteria. First, it should solve the vertical component of both the shallow-ice approximation and the shallow-shelf approximation exactly. Second, the above should be possible without spatial subdivision in the vertical dimension. Third, the number of basis functions should be as small as possible.

Finally, the basis functions should be orthogonal. One such choice of vertical basis functions which satisfies the above criteria is

$$\phi_0 = 1$$
$$\phi_1 = \frac{1}{p}\left[(p+1)\varsigma^p - 1\right] \tag{A3}$$

where p is the polynomial degree of the trial solution. Under the Galerkin approximation, this implies that the vertical structure of the horizontal velocity will be approximated by

$$u(\varsigma) = u_0 + \frac{u_1}{p}\left[(p+1)\varsigma^p - 1\right]. \tag{A4}$$

This represents an ansatz solution: we explicitly assume that the solution to the LMLa model is a linear combination of solutions to the shallow-shelf and shallow-ice models.

In the horizontal dimension, we use linear Lagrange finite elements ψ. The horizontal and vertical basis sets can be combined via tensor product, yielding the test function

$$\Pi^h(\hat{x},\hat{y},\varsigma) = \sum_{i=0}^{M} \Pi^h(\hat{x}_i,\hat{y}_i,0)\psi_i(\hat{x},\hat{y})(\phi_0 + \phi_1(\varsigma)), \tag{A5}$$

with test space

$$V^h = \text{span}\left\{\sum_{i=1}^{M}(\phi_0 + \phi_1(\varsigma))\psi_i(\hat{x},\hat{y})\right\}, \tag{A6}$$

where M is total number of horizontal grid locations. We then seek the function

$$\vec{u}^h \in U^h \,:\, u^h(\hat{x},\hat{y},\varsigma) = \sum_{i=1}^{M}\psi_i(u_{0i}\phi_0 + u_{1i}\phi_1) \tag{A7}$$

that satisfies

$$\int_{\bar{\Omega}}\int_1^0 \left[\bar{\nabla}\Pi^h + \partial_\varsigma \Pi^h \nabla\varsigma\right]\cdot 2\eta\dot{\epsilon}^h H \mathrm{d}\varsigma\mathrm{d}\bar{\Omega}$$
$$+ \int_{\bar{\Omega}}[\Pi^h \cdot f(\vec{u},T,H)]|_1 \mathrm{d}\bar{\Omega} - \int_{\bar{\Omega}}\int_1^0 \Pi^h\cdot\vec{\tau}_d \mathrm{d}\varsigma\mathrm{d}\bar{\Omega}, \tag{A8}$$
$$\forall \Pi^h \in V^h. \tag{A9}$$

We perform numerical integration in the horizontal dimension using a fourth-order quadrature rule. Accuracy of the numerical method in the vertical dimension relies on using a quadrature rule of sufficient order to integrate the trial functions exactly. In this case we use Gauss-Legendre quadrature over the half interval, which for polynomial degree p requires at least $n_q = (p+1)/4 + 1$ quadrature points.

A5. Alternate Basis Choices

With different choices of vertical basis functions, we can formulate different schemes. For example, if we make the choice

$$\phi_i(\varsigma) = T_i(\varsigma) \quad i \in [1,2,\ldots,p], \tag{A10}$$

where T_i is the ith degree Legendre polynomial [e.g., *Boyd*, 2001], we recover a Legendre spectral method. Conversely, if we take

$$\phi_0 = 1$$
$$\phi_1 = \delta(\varsigma - 1) \tag{A11}$$

and use only one numerical quadrature point, then we recover the L1L2 stress balance.

A6. Selecting *p*

We do not use a complete trial space (as would a true spectral method) for discretization of the vertical dimension. Rather than selecting a basis set of polynomials that can represent all polynomials up to degree γ

(a canonical example being the Legendre polynomials), we use a truncated pairing of two orthogonal polynomials selected a priori under the assumption that they can represent the solution with reasonable accuracy. In particular, we made the assumption that a linear combination of the vertically constant (SSA) and shallow-ice solutions is a good approximation. In the isothermal case, using the shape of the SIA solution as a basis function is straightforward: analytical results indicate that the polynomial degree of the curve is $n+1$, which implies that $p = n + 1$. We note here that this is an approximation; the inclusion of membrane stresses modifies this value. However, in shallow situations, this modification is of second order, and in plug flow it is irrelevant. We defer analysis of its importance in intermediate cases to intercomparison.

In the polythermal case, this approximation is less straightforward, since the SIA solution contains an integral, and this integral generally does not produce a polynomial. Including an integral in the basis set is complex and costly. Therefore, we introduce a further heuristic approximation of the thermomechanically coupled shallow-ice solution. We seek the polynomial p, such that the ratio of depth averaged to surface velocity is the same as for the shallow-ice solution. This implies that

$$\hat{u}_d(\hat{x},\hat{y}) = \frac{\int_0^1 A(T(\hat{x},\hat{y})^*)\varsigma^{n+1}\mathrm{d}\varsigma}{\int_0^A (T(\hat{x},\hat{y})^*)\varsigma^n \mathrm{d}\bar{\Omega}} \tag{A12}$$

$$p(\hat{x},\hat{y}) = -\frac{\hat{u}_d(\hat{x},\hat{y})}{\hat{u}_d(\hat{x},\hat{y}) - 1}. \tag{A13}$$

For an ice hardness parameter that is monomial in ς, the value of p will produce an exact correspondence to the shallow-ice solution. In the much more common case where A is something else entirely, the polynomial profile generally approximates the true SIA profile closely. For polythermal ice sheets, the value of p is often greater than 20. For such a profile, almost all of the shear is occurring near the base of the ice. This implies that using a traditional finite element or finite difference scheme requires high spatial resolution at the base. We circumvent this computationally intensive requirement by assuming a solution that fundamentally captures this variability.

Due to the heuristic nature of our discretization (in particular, the lack of completeness), it is difficult to obtain formal error estimates of the scheme. In general, assessments of numerical accuracy follow from evaluation of error against an analytical result under refinement of either mesh size or element order. The former makes sense in the horizontal dimension, where the mesh size can be iteratively reduced. However, we do not use a mesh for the vertical discretization, and we cannot increase the order of accuracy of the ansatz. Instead we rely on intercomparison and show that the present numerical method produces results which are comparable to the vertically discretized LMLa equations in all cases.

A7. Ice Sheet Model Intercomparison Project - Higher Order Model (ISMIP-HOM)

The ISMIP-HOM experiments [*Pattyn et al.*, 2008] are a series of benchmarks for comparing higher-order stress balance schemes for ice sheet models. ISMIP-HOM A and B are characterized by a nonslip basal boundary condition and sinusoidally varying basal topography, with a flat surface which constantly slopes in one direction. ISMIP-HOM A has bedrock variations in direction transverse to surface slope, while ISMIP-HOM B does not. Conversely, ISMIP-HOM C and D hold the basal topography constant while introducing basal sliding with a sinusoidally varying basal traction in one (ISMIP-HOM D) or both (ISMIP-HOM C) horizontal directions. All experiments have periodic lateral boundary conditions and are run at six wavelengths, ranging from 5 to 160 km.

Figure A1 compares the output from the model outlined above with the ISMIP-HOM benchmarks. In Figure A1, we also compare the heuristic ansatz with a full spectral method and an L1L2 scheme. The present method is comparable to both the LMLa models that took part in the intercomparison, as well as the spectral method. Indeed, it produces results more similar to the Stokes equations than the L1L2 model in the short-wavelength/low slip case that has stymied hybrid schemes.

A8. Numerical Solution of the Energy Balance

Vertically parameterized models have typically not treated temperature in a coupled way, either casting the problem in terms of vertically averaged temperature [*Sergienko*, 2014] or importing the temperature field from a vertically explicit model. This has been the case because the vertical structure of strongly advective

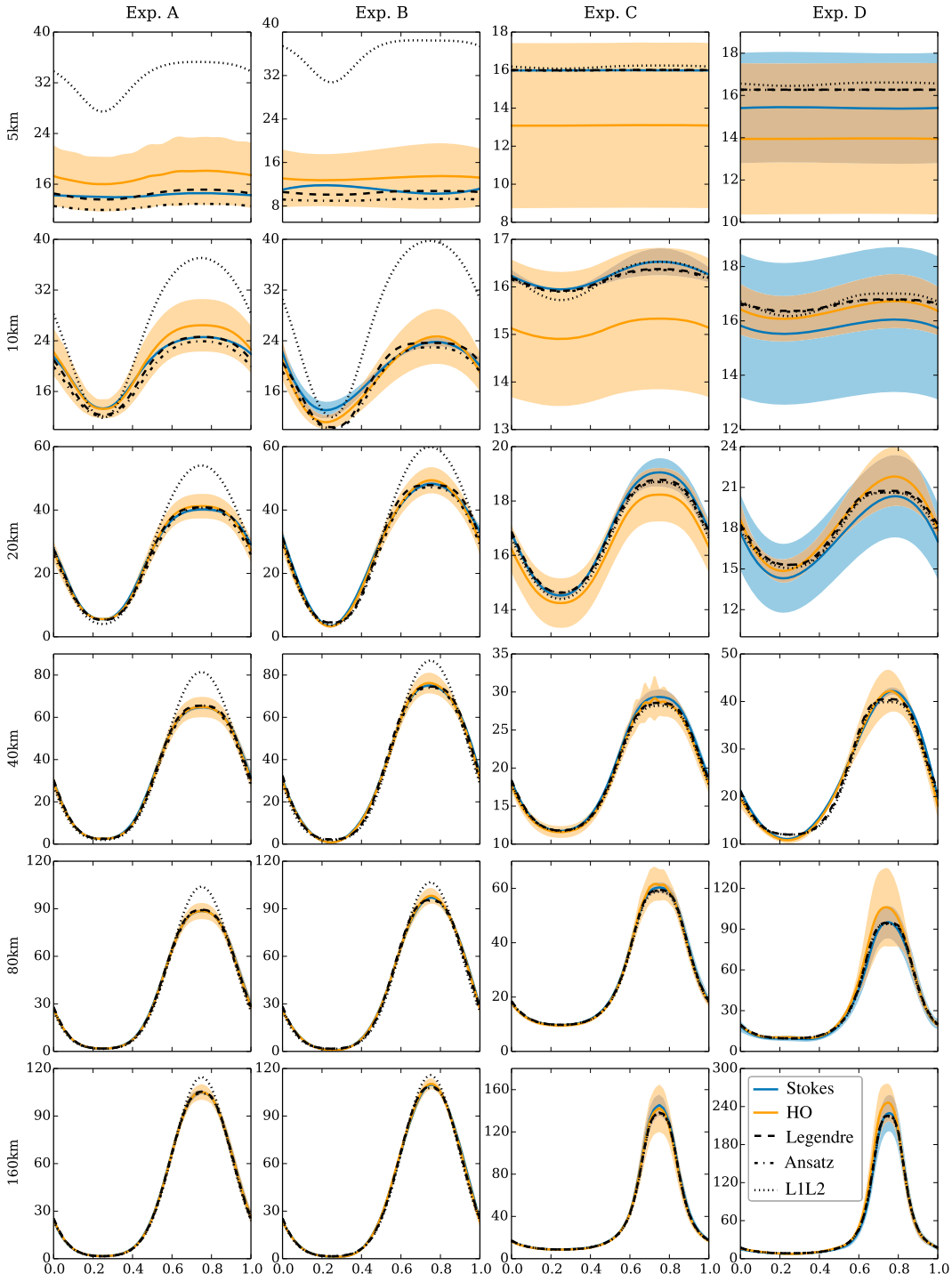

Figure A1. ISMIP-HOM benchmark results.

temperature fields cannot be readily approximated by a power series or other heuristic device [*Oerlemans*, 1982]. In the contemporary literature, there is no hybrid-type scheme for the energy balance.

Hence, we must solve the vertically explicit temperature equation; however, the computational cost required to solve the temperature equation is typically much smaller than that of the stress balance. Nonetheless, the overhead associated with forming a vertically explicit mesh and interpolating the velocity and temperature fields back and forth between nonmatching meshes is undesirable. We notice that finite element models for

ice sheet temperature often use an unstructured mesh in the horizontal and a structured mesh in the vertical [e.g., *Brinkerhoff and Johnson*, 2013; *Larour et al.*, 2012]. With a structured vertical mesh, parameterization of vertical layers is straightforward with the finite difference method while still retaining an unstructured mesh in the horizontal.

A9. Vertical Discretization With the Finite Difference Method

We seek to solve the temperature field at n_l equally spaced layers and assume that we can construct a good interpolant between them (linear interpolation is sufficient for our purposes).

We assume that the horizontal dimension will be discretized via the finite element method later. Now, we divide equation (9) into n_l vertical layers, as in the finite difference method, i.e., $T_i(x)$ for $i \in n_l$. We thus rewrite equation (9) as

$$\partial_t T_i + \vec{u}_i \cdot \nabla T_i + w_i^e \frac{T_{i+1} - T_{i-1}}{2\Delta\varsigma_i} = \kappa(\partial_z \varsigma)^2 \frac{T_{i-1} - 2T_i + T_{i+1}}{\Delta\varsigma_i^2} + \frac{\Phi_i}{\rho C_p}$$

$$\kappa \partial_z \varsigma \frac{T_1 - T_0}{\Delta\varsigma_0} = \alpha(T_0 - T_s) \tag{A14}$$

$$\kappa \partial_z \varsigma \frac{T_{n_l} - T_{n_l - 1}}{\Delta\varsigma_{n_l}} = q_g + q_f. \tag{A15}$$

where $\Delta\varsigma$ is the thickness of each layer, or $\frac{1}{n_l - 1}$ in ς coordinates, and functions subscripted with i are understood to be the function evaluated at ς corresponding to the ith layer. Also, we have defined an effective vertical velocity $w^e(\varsigma)$, which includes the effects of spatial and temporal changes in ς and is defined as

$$w^e(\varsigma) = \vec{u}(\varsigma) \cdot \nabla\varsigma + w\partial_z(\varsigma)\varsigma + \partial_t\varsigma. \tag{A16}$$

A10. Weak Form and Finite Element Discretization

Equation (A17) has already been discretized in the vertical dimension. Now we focus on discretization in time and horizontal space. For time discretization, we use a semi-implicit Crank-Nicholson scheme. The high Peclet number in the horizontal dimension introduces numerical instability under the Galerkin approximation. We circumvent this through streamline upwinding [*Brooks and Hughes*, 1982]. The variational problem is to find $T \in X$ such that

$$\begin{aligned}\sum_{i=2}^{nl-1} \int_\Omega \Bigg[& \zeta_i \frac{T_i^{j+1} - T_i^j}{\Delta t} + \left(\zeta_i + \tau_i \vec{u}_i \cdot \nabla\zeta_i\right)\left(\vec{u}_i \cdot \nabla T_i^{j+\theta}\right) \\ & + \zeta_i w_i^e \frac{T_{i+1}^{j+\theta} - T_{i-1}^{j+\theta}}{2\Delta\varsigma_i} \\ & - \zeta_i \left(\kappa(\partial_z\varsigma)^2 \frac{T_{i+1}^{j+\theta} - 2T_i^{j+\theta} + T_{i-1}^{j+\theta}}{\Delta\varsigma_i^2} + \frac{\Phi_i}{\rho C_p} \right) \Bigg] \mathrm{d}\Omega \\ & + \int_\Omega \zeta_0 \left[\kappa \partial_z \varsigma \frac{T_1^{j+\theta} - T_0^{j+\theta}}{\Delta\varsigma_0} - \alpha\left(T_{n_l}^{j+\theta} - T_s\right) \right] \mathrm{d}\Omega \end{aligned} \tag{A17}$$

$$- \int_\Omega \zeta_1 \left[\kappa \partial_z \varsigma \frac{T_{n_l - 1}^{j+\theta} - T_{n_l - 2}^{j+\theta}}{\Delta\varsigma_{n_l}} + (q_g + q_f) \right] \mathrm{d}\Omega = 0, \quad \forall \zeta \in X, \tag{A18}$$

where $X = H^1(\bar{\Omega})^{n_l}$. We discretize the above using linear lagrange elements and a fourth-order quadrature scheme over the elements.

This equation is weakly nonlinear in the strain heating term and subject to an inequality constraint. In order to deal with the former, we linearize the strain heating term about the current time step and treat it explicitly. In order to deal with the latter, we make an unconstrained time step and then set values that go above the pressure melting point to be equal to it. This is somewhat crude but is simple and commonly used throughout the literature [e.g., *Bueler et al.*, 2007].

A11. Numerical Solution of the Transport Equation

Ostensibly, the transport equation (8) is hyperbolic; however, this belies the fact that the fluxes are nonlinearly dependent both upon the gradient of the thickness and the thickness itself. Additionally, it is subject to the additional constraint that thickness remains positive, even in the presence of a strongly negative source term.

Velocity is primarily a function of surface slope. In the shallow-ice context where velocity is *only* a function of surface slope and thickness, mass transport becomes nonlinearly diffusive. This diffusive character possesses desirable numerical properties in terms of managing discontinuities and "wiggles." The same is true for motion only due to basal sliding. The inclusion of longitudinal stresses induces advective terms, which, for grounded ice, are small. In order to take advantage of this diffusive dominance, we decompose the velocity into two components: the shallow-ice solution and the velocity components due to nonshallow effects (e.g., longitudinal coupling)

$$\bar{u} = \bar{u}_{\mathrm{SIA}} + \bar{u}_c. \tag{A19}$$

$\bar{u}_c$ can be evaluated inexpensively after solving the momentum balance, as $\bar{u}_{\mathrm{SIA}}$ is a simple computation. Substituting these into the transport equation yields

$$H_t - \bar{\nabla} \cdot \left[D(H)\bar{\nabla} S - \bar{u}_c \cdot H \right] = \dot{a}. \tag{A20}$$

where D is the standard shallow-ice approximation nonlinear diffusion term [*Hindmarsh*, 2001].

A12. Discretization and Solution Procedure

We discretize in time using an implicit-explicit θ method [e.g., *Zienkiewicz and Taylor*, 2000], where the diffusive term is discretized implicitly and the advective term explicitly. The advective term is also stabilized with isotropic diffusion; note, however, that isotropic diffusion in this context approximates streamline diffusion, since the velocity vectors are oriented nearly parallel to the surface gradient. Where this statement does not hold, either surface gradients are small (meaning that there is commensurately little artificial diffusion) or some crosswind diffusion is desirable for stability purposes. The variational problem is then to find $H \in Z$ such that

$$\begin{aligned} &\int_\Omega \left[\xi \frac{H^{n+1} - H^n}{\Delta t} - \nabla \xi \cdot D(H^{n+\theta}) \nabla H^{n+\theta} \right. \\ &\left. -\nabla \xi \cdot \bar{u}_c H^n - \tau(\bar{u}_c \cdot \bar{u}_c) \nabla \xi \cdot \nabla H^n - \xi \dot{a} \right] \mathrm{d}\Omega = 0, \\ &\forall \xi \in Z, \end{aligned} \tag{A21}$$

where $Z = H^1(\bar{\Omega})$ and τ is a stabilization parameter given by

$$\tau = \frac{\gamma h}{2|\vec{u}|} \tag{A22}$$

$$\gamma = \coth |\mathrm{Pe}| - \frac{1}{|\mathrm{Pe}|} \tag{A23}$$

$$\mathrm{Pe} = \frac{h \bar{u}_c}{D} \tag{A24}$$

and h is the local element circumradius. We discretize using linear Lagrange elements and a fourth-order quadrature rule. This equation is nonlinear in H, and we use an active set Newton's method in order to find the solution while respecting the constraint of positive thickness [*Balay et al.*, 2014]. The Jacobian of this system is computed analytically with respect to H^{n+1}. We have found that linearizing the diffusion coefficient about H^n and treating the system as linear introduces a numerical instability and that solving the full nonlinear system helps to avoid this. Following *Hindmarsh and Payne* [1996], we choose $\theta = \frac{3}{2}$ for maximum stability.

Acknowledgments
This work was supported by NASAgrant NNX11AM12A and NASAgrant NNX11AR23G. We acknowledge Andy Aschwanden for the discussions and review that greatly improved the quality of this manuscript. We also gratefully acknowledge Heinz Blatter, Jonathan Kingslake, and an anonymous reviewer, all of whom provided insightful and interesting commentary which greatly improved the quality of this manuscript. Model code relevant to the production of the results contained herein is available at https://github.com/douglas-brinkerhoff/hybrid-streaming.

References

Alley, R. B., and S. Anandakrishnan (1994), A water-piracy hypothesis for the anandakrishnan: 1997b of ice stream C, Antarctica, *Ann. Glaciol.*, *20*, 187–194.
Balay, S., et al. (2014), PETSc users manual, *Tech. Rep. ANL-95/11 - Revision 3.5*, Argonne Nat. Lab., Chicago, Ill.
Bamber, J. L., D. G. Vaughan, and I. Joughin (2000), Widespread complex flow in the interior of the Antarctic Ice Sheet, *Science*, *287*(5456), 1248–1250.
Banks, J., J. Brooks, G. Cairns, G. Davis, and P. Stacey (1992), On Devaney's definition of chaos, *Am. Math. Mon.*, *99*(4), 332–334.
Bassis, J. N. (2010), Hamilton's principle applied to ice sheet dynamics: New approximations for the large-scale flow of ice sheets, *J. Glacial.*, *56*(97), 497–513.
Bindschadler, R., and P. Vornberger (1998), Changes in the West Antarctic Ice Sheet since 1963 from declassified satellite photography, *Science*, *279*(5351), 689–692.
Bougamont, M., S. Tulaczyk, and I. R. Joughin (2003), Response of subglacial sediments to basal freeze-on 2. Application in numerical modeling of the recent stoppage of Ice Stream C, West Antarctica, *J. Geophys. Res.*, *108*(B4), 2223, doi:10.1029/2002JB001936.
Boyd, J. P. (2001), *Chebyshev and Fourier Spectral Methods*, 2nd ed., Dover, New York.
Brinkerhoff, D. J., and J. V. Johnson (2013), Data assimilation and prognostic whole ice sheet modelling with the variationally derived, higher order, open source, and fully parallel ice sheet model VarGlaS, *Cryosphere*, *7*(4), 1161–1184, doi:10.5194/tc-7-1161-2013.
Brooks, A. N., and T. J. Hughes (1982), Streamline upwind/Petrov-Galerkin formulations for convection dominated flows with particular emphasis on the incompressible Navier-Stokes equations, *Comput. Meth. Appl. Mech. Eng.*, *32*(1–3), 199–259, doi:10.1016/0045-7825(82)90071-8.
Bueler, E., and J. Brown (2009), Shallow shelf approximation as a "sliding law" in a thermomechanically coupled ice sheet model, *J. Geophys. Res.*, *114*, F03008, doi:10.1029/2008JF001179.
Bueler, E., J. Brown, and C. Lingle (2007), Exact solutions to the thermomechanically coupled shallow-ice approximation: Effective tools for verification, *J. Glaciol.*, *53*(182), 499–516.
Conway, H., G. Catania, C. F. Raymond, A. M. Gades, T. A. Scambos, and H. Engelhardt (2002), Switch of flow direction in an Antarctic ice stream, *Nature*, *419*(6906), 465–467.
DeGrood, M. H., and M. J. Schervish (2011), *Probability and Statistics*, 4th ed., Pearson, New York.
Echelmeyer, K. A., and W. D. Harrison (1999), Ongoing margin migration of Ice Stream B, Antarctica, *J. Glaciol.*, *45*(150), 361–369.
Echelmeyer, K. A., T. S. Clarke, and W. D. Harrison (1991), Surficial glaciology of Jakobshavns Isbrae, West Greenland, *J. Glaciol.*, *37*, 368–382.
Flowers, G. E. (2015), Modelling water flow under glaciers and ice sheets, *Proc. R. Soc. London, Ser. A*, *471*, 2176, doi:10.1098/rspa.2014.0907.
Fowler, A. (2001), Modelling the flow of glaciers and ice sheets, in *Continuum Mechanics and Applications in Geophysics and the Environment*, edited by B. Straughan et al., pp. 201–221, Springer, Berlin.
Fowler, A. G., and L. E. Schiavi (1998), A theory of ice-sheet surges, *J. Glaciol.*, *44*, 104–118.
Geuzaine, C., and J.-F. Remacle (2009), GMSH: A 3-D finite element mesh generator with built-in pre- and post-processing facilities, *Int. J. Numer. Methods Eng.*, *79*(11), 1309–1331, doi:10.1002/nme.2579.
Goldberg, D. N., and O. V. Sergienko (2011), Data assimilation using a hybrid ice flow model, *Cryosphere*, *5*(2), 315–327, doi:10.5194/tc-5-315-2011.
Hindmarsh, R. C. A. (2001), Influence of channelling on heating in ice-sheet flows, *Geophys. Res. Lett.*, *28*(19), 3681–3684.
Hindmarsh, R. C. A. (2004a), Thermoviscous stability of ice-sheet flows, *J. Fluid Mech.*, *502*, 17–40, doi:10.1017/S0022112003007390.
Hindmarsh, R. C. A. (2004b), A numerical comparison of approximations to the Stokes equations used in ice sheet and glacier modeling, *J. Geophys. Res.*, *109*, F01012, doi:10.1029/2003JF000065.
Hindmarsh, R. C. A. (2009), Consistent generation of ice-streams via thermo-viscous instabilities modulated by membrane stresses, *Geophys. Res. Lett.*, *36*, L06502, doi:10.1029/2008GL036877.
Hindmarsh, R. C. A., and A. J. Payne (1996), Time-step limits for stable solutions of the ice-sheet equation, *Ann. Glaciol.*, *23*, 74–85.
Hulbe, C., and M. Fahnestock (2007), Century-scale discharge stagnation and reactivation of the Ross Ice Streams, West Antarctica, *J. Geophys. Res.*, *112*, F03S27, doi:10.1029/2006JF000603.
Joughin, I., and S. Tulaczyk (2002), Positive mass balance of Ross Ice Streams, West Antarctica, *Science*, *295*, 476–480.
Joughin, I., S. Tulaczyk, R. Bindschadler, and S. F. Price (2002), Changes in West Antarctic Ice Stream velocities: Observation and analysis, *J. Geophys. Res.*, *107*(B11), 2289, doi:10.1029/2001JB001029.
Joughin, I., et al. (2005), Continued deceleration of Whillans Ice Stream, West Antarctica, *Geophys. Res. Lett.*, *32*, L22501, doi:10.1029/2005GL024319.
Kingslake, J. (2015), Chaotic dynamics of a glaciohydraulic model, *J. Glaciol.*, *61*(227), 493–502, doi:10.3189/2015JoG14J208.
Larour, E., H. Seroussi, M. Morlighem, and E. Rignot (2012), Continental scale, high order, high spatial resolution, ice sheet modeling using the Ice Sheet System Model (ISSM), *J. Geophys. Res.*, *117*, F01022, doi:10.1029/2011JF002140.
Logg, A., K.-A. Mardal, and G. N. Wells (Eds.) (2012), *Automated Solution of Differential Equations by the Finite Element Method*, Springer, New York, doi:10.1007/978-3-642-23099-8.
Muskett, R. R., C. S. Lingle, J. M. Sauber, A. S. Post, W. V. Tangborn, and B. T. Rabus (2008), Surging, accelerating surface lowering and volume reduction of the Malaspina Glacier system, Alaska, USA, and Yukon, Canada, from 1972 to 2006, *J. Glaciol.*, *54*(188), 788–800, doi:10.3189/002214308787779915.
Oerlemans, J. (1982), Glacial cycles and ice-sheet modelling, *Clim. Change*, *4*, 353–374.
Oppenheimer, M. (1998), Global warming and the stability of the West Antarctic Ice Sheet, *Nature*, *393*, 325–332.
Orsi, A. J., B. D. Cornuelle, and J. P. Severinghaus (2012), Little ice age cold interval in West Antarctica: Evidence from borehole temperature at the West Antarctic Ice Sheet (WAIS) divide, *Geophys. Res. Lett.*, *39*, L09710, doi:10.1029/2012GL051260.
Pattyn, F. (2003), A new three-dimensional higher-order thermomechanical ice sheet model: Basic sensitivity, ice stream development, and ice flow across subglacial lakes, *J. Geophys. Res.*, *108*(B8), 2382, doi:10.1029/2002JB002329.
Pattyn, F., et al. (2008), Benchmark experiments for higher-order and full-Stokes ice sheet models (ISMIP-HOM), *Cryosphere*, *2*(2), 95–108, doi:10.5194/tc-2-95-2008.
Payne, A. J. (1995), Limit cycles in the basal thermal regime of ice sheets, *J. Geophys. Res.*, *100*(B3), 4249–4263.
Payne, A. J., and P. W. Dongelmans (1997), Self-organisation in the thermomechanical flow of ice sheets, *J. Geophys. Res.*, *102*(B6), 12,219–12,234.
Payne, A. J., P. Huybrechts, A. Abe-Oughi, J. L. F. R. Calov, R. Greve, S. J. Marshall, I. Marsiat, C. Ritz, L. Tarasov, and M. P. A. Thomassen (2000), Results from the EISMINT model intercomparison: The effect of thermomechanical coupling, *J. Glaciol.*, *46*, 227–238.
Pollard, D., and R. M. DeConto (2012), Description of a hybrid ice sheet-shelf model, and application to Antarctica, *Geosci. Model Dev.*, *5*(5), 1273–1295, doi:10.5194/gmd-5-1273-2012.

Price, S., R. Bindschadler, C. Hulbe, and I. Joughin (2001), Post-stagnation behavior in the upstream regions of Ice Stream C, West Antarctica, *J. Glaciol.*, *47*(157), 283–294, doi:10.3189/172756501781832232.

Retzlaff, R., and C. R. Bentley (1993), Timing of stagnation of Ice Stream C, West Antarctica from short-pulse radar studies of buried surface crevasses, *J. Glaciol.*, *39*(133), 553–561.

Rignot, E. J., and R. H. Thomas (2002), Mass balance of polar ice sheets, *Science*, *297*(5586), 1502–1506.

Saito, F., A. Abe-Ouchi, and H. Blatter (2006), European Ice Sheet Modelling Initiative (EISMINT) model intercomparison experiments with first-order mechanics, *J. Geophys. Res.*, *111*, F02012, doi:10.1029/2004JF000273.

Sayag, R., and E. Tziperman (2008), Spontaneous generation of pure ice streams via flow instability: Role of longitudinal shear stresses and subglacial till, *J. Geophys. Res.*, *113*, B05411, doi:10.1029/2007JB005228.

Sayag, R., and E. Tziperman (2011), Interaction and variability of ice streams under a triple-valued sliding law and non-Newtonian rheology, *J. Geophys. Res.*, *116*, F01009, doi:10.1029/2010JF001839.

Schoof, C., and R. Hindmarsh (2010), Thin-film flows with wall slip: An asymptotic analysis of higher order glacier flow models, *Q. J. Appl. Math.*, *63*(1), 73–114.

Sergienko, O. V. (2014), A vertically integrated treatment of ice stream and ice shelf thermodynamics, *J. Geophys. Res. Earth Surf.*, *119*, 745–757, doi:10.1002/2013JF002908.

Seybold, H., J. S. Andrade, and H. J. Herrmann (2007), Modeling river delta formation, *Proc. Natl. Acad. Sci. U.S.A.*, *104*(43), 16,804–16,809, doi:10.1073/pnas.0705265104.

Stokes, C. R., and L. Tarasov (2010), Ice streaming in the laurentide ice sheet: A first comparison between data-calibrated numerical model output and geological evidence, *Geophys. Res. Lett.*, *37*, L01501, doi:10.1029/2009GL040990.

Truffer, M., and K. A. Echelmeyer (2003), Of isbræ and ice streams., *Ann. Glaciol.*, *36*, 66–72.

Tulaczyk, S., W. B. Kamb, and H. F. Engelhardt (2000), Basal mechanics of Ice Stream B, West Antarctica 2. Undrained plastic bed model, *J. Geophys. Res.*, *105*(B1), 483–494.

Turcotte, D. (1997), *Fractals and Chaos in Geology and Geophysics*, 2nd ed., Cambridge Univ. Press, Cambridge, U. K.

Welch, P. D. (1967), The use of fast Fourier transform for the estimation of power spectra: A method based on time averaging over short, modified periodograms, *IEEE Trans. Audio Electroacoust.*, *15*(2), 70–73, doi:10.1109/TAU.1967.1161901.

Werder, M. A., I. J. Hewitt, C. G. Schoof, and G. E. Flowers (2013), Modeling channelized and distributed subglacial drainage in two dimensions, *J. Geophys. Res. Earth Surf.*, *118*, 2140–2158, doi:10.1002/jgrf.20146.

Zienkiewicz, O. C., and R. L. Taylor (2000), *The Finite Element Method,* 5th ed., Butterworth-Heinemann, Oxford, U. K.